LAWRENCE
LIVERMORE
NATIONAL
LABORATORY

LLNL-TR-703869

Final Report: Rational Design of Wide Band Gap Buffer Layers for High-Efficiency Thin-Film Photovoltaics

V. Lordi

September 27, 2016

Disclaimer

This work performed under the auspices of the U.S. Department of Energy by Lawrence Livermore National Laboratory under Contract DE-AC52-07NA27344.

Final Report

Project Title:	Rational Design of Wide Band Gap Buffer Layers for High-Efficiency Thin-Film Photovoltaics
Project Period:	01/01/13 – 9/30/16
Project Budget:	$900,000
Submission Date:	9/30/16
Recipient:	Lawrence Livermore National Laboratory
Address:	7000 East Ave Livermore, CA 94550
Award Number:	CPS25853
Project Team:	University of Illinois, MiaSolé Hi-Tech
Contacts:	Vincenzo Lordi Staff Scientist and Deputy Group Leader Phone: 925-423-2755 Email: lordi2@llnl.gov

This work was performed under the auspices of the U.S. Department of Energy by Lawrence Livermore National Laboratory under Contract DE-AC52-07NA27344.

LLNL-TR-703869

Executive Summary

The main objective of this project is to enable rational design of wide band gap buffer layer materials for CIGS thin-film PV by building understanding of the correlation of atomic-scale defects in the buffer layer and at the buffer/absorber interface with device electrical properties. Optimized wide band gap buffers are needed to reduce efficiency loss from parasitic absorption in the buffer. The approach uses first-principles materials simulations coupled with nanoscale analytical electron microscopy as well as device electrical characterization. Materials and devices are produced by an industrial partner in a manufacturing line to maximize relevance, with the goal of enabling R&D of new buffer layer compositions or deposition processes to push device efficiencies above 21%. Cadmium sulfide (CdS) is the reference material for analysis, as the prototypical high-performing buffer material.

Key findings include:

- Native defects in the bulk materials contribute to self-doping and self-compensation effects, which may limit dopability. For example, vacancy self-compensation severely limits the equilibrium *n*-type dopability of the wide band gap material ZnS, while CdS does not suffer from this problem. Impurities incorporated during film deposition, which differ depending on deposition technique, can promote desirable *n*-type conductivity in materials not suffering from strong native self-compensation.
- Conduction band offset (CBO) with respect to the absorber (CIGS) is a critical parameter for overall device performance. ZnS or CdZnS increases the CBO compared to CdS, which is detrimental if too large. This effect is related to the reason wider band gap CdZnS alloys are more difficult to dope *n*-type.
- Rapid sputter deposition in the MiaSolé Hi-Tech manufacturing line can be tuned to produce very crystalline, even epitaxial, buffer material. The crystallinity depends primarily on oxygen content in the sputter gas. Both zinc-blende and wurtzite phases of buffer may nucleate and grow, dependent on the exposed facet of the CIGS below. Oxygen and/or zinc incorporation occurs in some conditions.
- Intermixing at the absorber/buffer interface is critically important and can be controlled by process gases during deposition, particularly oxygen. A buried homojunction in the absorber can be promoted by causing counter-doping of Cu from CIGS and Cd from the buffer across the interface. Certain process conditions promote secondary phase formation near the interface, including Cu_2S phases.
- Alloying provides opportunities for multi-objective optimization of the buffer material across band gap, CBO, dopability, interface quality, and film crystallinity. (Cd,Zn)(O,S) and (Cd,Mg)(O,S) alloy systems were found to have fairly narrow optimal ranges of composition consistent with experiments. There is opportunity for alternative optima, which require very high buffer doping, but circumvent the need for small CBO. Secondary phase formation also is possible in these alloy systems, due to tendencies to phase separate at modest temperatures.

Table of Contents

Background

Historically, champion-efficiency CIGS photovoltaic devices produced in the laboratory have utilized CdS buffer layers between the absorber and transparent contact layer.[1,2,3] Efficiency loss analyses for CIGS devices shows significant current loss from the typical CdS buffer due to its direct bandgap in the blue end of the solar spectrum (~2.4 eV) and near-zero collection efficiency of electron-hole pairs generated in this layer, representing a major limiter of device efficiency.[4] This problem is compounded in commercially manufactured PV panels because the CdS buffer layer generally must be thicker than in record-efficiency laboratory devices, to ensure large area coverage and prevent shunting pathways.[5] As a result, much effort has been placed in seeking to replace CdS with a wider band gap alternative, such as ZnS, $Cd_{1-x}Zn_xS$, or ZnO.[6,7] However, alternative buffers generally have caused either lower open-circuit voltage[8] or lower fill factor[9] and thus degraded efficiency.

Investigations have shown a number of requirements to enable high efficiency devices. First, it has been proposed theoretically that a negative conduction band offset from the absorber to the buffer layer can lower device performance by enhancing interface recombination.[10] Several groups have shown evidence for such a negative band offset with buffer layers such as ZnO,[11] for example, which explained poor efficiencies of those devices. Alternatively, theory has shown that very large positive conduction band offsets (>0.4 eV) at the buffer/absorber interface can create a double-diode behavior[12] that also can reduce device performance. It has further been suggested that increased interface recombination due to either Fermi-level pinning or increased concentrations of interfacial recombination centers can reduce device efficiencies when using buffer layers other than CdS,[13] although the nature of such interfacial defects has not been determined. Finally, it has been proposed that a CdS layer is necessary to fabricate high-performance devices by creating a pseudo-homojunction in the absorber layer, thereby minimizing recombination at the hetero-interface,[14] but this has not been shown to be true in general.

An additional complication for using alternative buffer layers in commercial thin-film PV processes is related to electrical metastabilities that have been observed to occur when using non-CdS buffer layers.[6] Typical manifestations of these metastabilities include strong dependence of performance on light-soaking,[15] thermal treatments,[6] and wavelength of illumination.[16] These effects sometimes also occur in CdS-based devices,[17,18,19] but the impact on the measured device efficiency is generally much smaller than for alternative buffers. In a manufacturing setting, where every panel has to be flashed quickly to determine its rated power, it becomes increasingly problematic to handle metastable devices without either de-rating panels or employing expensive light soaking procedures, both options that increase the cost per kWh.

Introduction

This project aims to achieve leap-ahead efficiency of manufacturable thin-film solar cells by developing advanced buffer layer materials. Large-scale first-principles materials simulations coupled closely with advanced experimental characterization will be combined with the manufacturing and device expertise of MiaSolé Hi-Tech, a leading

industrial producer of CIGS solar cells, to enable the design of high-performance materials. Understanding the correlations of composition and deposition conditions with interface defects, current-loss, and fill factor degradation will enable fabrication of new buffer layers that can achieve near-theoretical cell efficiency. Opportunity exists to improve cell efficiency by up to 3% absolute.

The novelty of the research is to combine basic and applied science expertise at the national labs and universities with state-of-the-art manufacturing and synthesis in industry. By identifying the underlying causes and mechanisms of sub-optimal performance of existing wide band gap buffer alternatives to CdS, we will enable rational design of new materials and/or processes for optimal performance.

Summary Task List:

Task 1: Calculate properties of intrinsic defects and impurities in bulk CdS
Milestone (Task 1): Report on theoretical nature of defects in bulk CdS

Task 2: Calculate properties of CdS/CIGS interface
Milestone (Task 2): Report on CdS/CIGS interface electronic states

Task 3: Sample fabrication — CdS/CIGS

Task 4: Sample characterization — CdS/CIGS interface
Milestone (Task 4): Report spatially-resolved compositional analyses of at least two representative samples of CdS/CIGS interface

Go/No-Go Decision Point (18 months): Upon successful validation of bulk materials models, continue to Phase 2 exploration of alloy materials

Task 6: Calculate effect of Zn and O alloying on bulk (Cd,Zn)(O,S) properties
Milestone (Task 6): Report on alloy effects on (Cd,Zn)(O,S) electronic properties

Task 7: Calculate effect of Zn and O alloying on (Cd,Zn)(O,S)/CIGS interface properties

Task 8: Sample fabrication — (Cd,Zn)(O,S)/CIGS

Task 9: Sample characterization — CdS/CIGS and (Cd,Zn)(O,S)/CIGS interfaces
Milestone 1 (Task 9): Correlate experiments with models
Milestone 2 (Task 9): Deliver publication on CdS/CIGS interface structure and electronic properties (joint theory and experiment)

Final Deliverables

FD1: Publication on CdZnS alloy electronic properties
FD2: Publication on (Cd,Zn)(O,S)/CIGS interface electronic properties
FD3: Report and publication or conference presentation on assessment of process/materials design options for high-performance wide band gap buffer layer

Project Results and Discussion

Methods

I. Computational Methods

As direct comparisons with experiment were very important throughout this project, we performed calculations employing state-of-the-art hybrid functional density functional theory to more accurately calculate a number of relevant properties of the buffer and absorber layers. This allowed us to obtain a much better description of the underlying electronic structure of the individual materials, energetics and details of the dominant intrinsic defects and common impurities in the buffer layers, and the influence of alloying in the buffer, which we detail more below.

All of the calculations are based on density functional theory with the Heyd-Scuseria-Ernzerhof (HSE06)[20] screened hybrid functional as implemented in the VASP code.[21] The HSE06 functional has become a popular and effective choice for reproducing experimental band gaps and providing a more accurate description of defect charge-state transition levels compared to those obtained with semilocal exchange correlation functionals within the generalized gradient (GGA) or local density (LDA) approximations. As shown in Figure 1 for CdS, we find that GGA (using the PBE functional as parameterized by Perdew, Burke, and Ernzerhof[22]) and HSE06 with the conventional fraction of 25% non-local Hartree-Fock (HF) exchange underestimate the band gaps of bulk CdS (although PBE much more severely than HSE06). Therefore, we modified the fraction of HF exchange to 32% for CdS and 36% for ZnS in the HSE functional to improve the representation of the bulk band gaps, valence bandwidths, and relative positions of the charge-state transition levels. The modified mixing also improves the description of the structure (lattice constants), as summarized in **Table I**. For band offset calculations, we modified the fraction of exact-exchange to 36% for ZnO and to 30% for both CISe and CGSe.

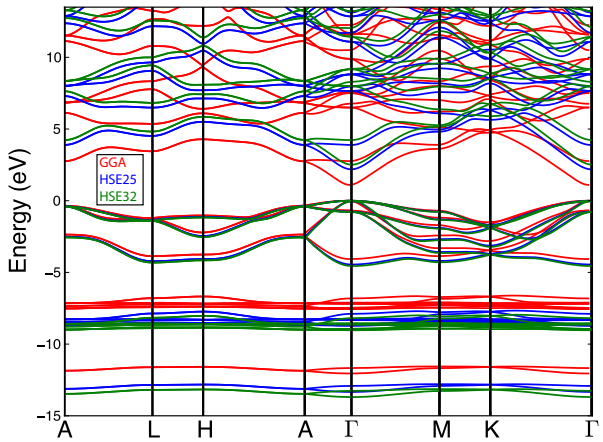

Figure 1. Band structure of CdS calculated with different levels of theory. Shown in red, the generalized gradient approximation (GGA) severely underestimates the band gap, whereas the HSE06 hybrid functional with 25% mixing leads to a significant improvement (HSE25, blue). The experimental band gap can be reproduced by incorporating a slightly larger fraction of 32% exact-exchange (HSE32, green). All defect calculations use 32% mixing.

Table I. The calculated structural parameters, band gaps, and formation enthalpies for wurtzite CdS and ZnS. The fraction of Hartree-Fock exchange (α) was modified for each material and is included in parenthesis, where 0% represents results obtained with GGA-PBE. Experimental values are included for comparison.

	CdS - wurtzite			**ZnS - wurtzite**		
	Calculated α =0%	Calculated α = 32%	Experiment	Calculated α =0%	Calculated α = 36%	Experiment
***a* (Å)**	4.20	4.17	4.14	3.85	3.83	3.82
***c* (Å)**	6.87	6.80	6.75	6.33	6.29	6.26

For defect calculations in the buffer layers, we used 96-atom supercells of the wurtzite phases of CdS and ZnS, and up to 216-atom supercells for the zincblende phases. For all calculations, the plane-wave expansion of wave functions uses an energy cutoff of 400 eV and Brillouin zone integrations use a 2×2×2 mesh of Monkhorst-Pack *k*-points. Correction of finite-size errors from the spurious periodic Coulomb interaction of charged defects were explicitly included following the scheme of Freysoldt et al.,[23] with a weighted spatially-averaged static dielectric constant of $8.4\varepsilon_0$ for CdS and $8.2\varepsilon_0$ for ZnS.[24] Convergence of results with respect to supercell size was verified.

We calculate defect formation energies (E^f) to determine the relative equilibrium concentrations of defects and impurities, the favorable charge states (q) for different conditions, and the charge-state transition levels (ε).[25] Using a specific case as an example, the formation energy of the sulfur vacancy (V_S) in CdS is given by

$$E^f[V_S^q] = E_{tot}[V_S^q] - E_{tot}[\mathrm{CdS}] + \mu_S + q\varepsilon_F \,, \qquad (1)$$

where $E_{tot}[V_S^q]$ and $E_{tot}[\mathrm{CdS}]$ represent, respectively, the total energy of the supercell containing the vacancy in charge state q, and that of a perfect crystal in the same supercell. The S removed from the crystal is placed in a reservoir referenced to the energy per atom of elemental sulfur. The chemical potential μ_S can vary to represent experimental conditions during growth or annealing, i.e. from Cd-rich to S-rich conditions. These limits are set by the formation enthalpy of CdS, which is included in **Table IV**. The chemical potential references for other relevant species are elemental *hcp* Cd and Zn. For the common impurities we studied, we considered references of molecular O_2, H_2, N_2, and diamond C. For the defects resulting from intermixing, we considered the energy per atom for bulk Se, Al, Ga, In, Sn, Cu, Na, and K. Each absorber- or window-layer-related impurity chemical potential was also bounded by formation of competing phases of CuS, SnS, Al_2S_3, Ga_2S_3, In_2S_3, ZnSe, and CdSe. Na and K were bounded by the Na_2S and K_2S phases. For charged defects, electrons are exchanged with a reservoir whose chemical potential is the Fermi level ε_F, which we reference to the valence band maximum (VBM). Analogous expressions apply for other defects and for defects in ZnS.

Migration barriers for the relevant native defects and intermixing-impurities were calculated using the climbing nudged elastic band (NEB) method.[26] The NEB path first

was optimized using PBE-GGA, then the energy barrier at the saddle-point configuration was evaluated with a single-shot HSE06 calculation. This approximation is expected to result in upper bounds of all migration barriers compared to the experimental values. To facilitate comparison with experiment, we estimate a minimum temperature for diffusion of a defect from the calculated activation energy (Ea) using transition state theory and assuming a minimum hopping rate $\Gamma = \Gamma_0 \exp[-E_a/k_BT]$ of one per minute, where Γ_0 is chosen as 10 THz for a value characteristic of the optical phonon modes in CdS.[24] This procedure leads to a value of 388 K/eV for converting the reported activation energies into an approximate onset temperature (T_a) for the reported diffusion processes.

To model the quaternary alloys, we adopt special quasi-random structures (SQS) that mimic the random alloy of a given composition.[27] We adopt SQS structures that have been previously published for *fcc* and *hcp* lattices to construct wurtzite, zincblende and rocksalt SQS.[28] The underlying SQS directly determine the alloy compositions that can be simulated. The hcp SQS structures can describe alloy compositions in increments of 25% (25%, 50%, and 75% binary alloys), while the available fcc SQS structures yield a finer resolution of 6.25%. When constructing the wurtzite SQS, this leads to a much coarser description of the quaternary (Cd,Zn)(O,S). The zincblende and rocksalt alloys have a much finer resolution over the composition space, leading to a total of $17^2 = 289$ unique alloy compositions that can be explicitly simulated. The zincblende phases therefore provide a more informative look at how small changes in stoichiometry can influence the underlying bulk properties.

Due to the difficulty in constructing explicit interfaces or surfaces to evaluate the band offsets as a function of stoichiometry, we base our band alignments on the branch-point energy (E_{BP}) evaluated for each composition. The branch-point energy, also referred to as the charge-neutrality level (CNL), represents an effective energy where the bulk states change from pre- dominantly valence-band-like or donor-like character to conduction-band-like or acceptor-like character. The concept of the E_{BP} or CNL has had tremendous success in providing a common reference level from which to align the unstrained band edges of semiconductors and insulators.[29] While various methods have been proposed to calculate the E_{BP} we adopt the approach of Schleife et al. that modified previous methodologies for determining this quantity from the bulk electronic structure,[30] which depends on the eigenvalues (ε) of the single- particle states, the chosen *k*-point sampling (i.e the particular wave vectors ***k*** and their total number, Nk), the number of included conduction band states (N_{CB}) and valence band states (N_{VB}). For our zincblende alloy supercells we consider all 8 irreducible *k*-points comprising the 2×2×2 Γ-centered *k*-point mesh. Schleife et al.[30] adopted a choice of N_{VB}=2 and N_{CB}=1 for the two- atom zincblende unit cell, which we scale to N_{VB}=64 and N_{CB}=32 for our 64-atom alloy supercells and N_{VB}=32 and N_{CB}=16 for our 32-atom supercells. This choice also leads to nearly identical results for the bulk supercell for each of CdO, CdS, ZnS, and ZnO as compared to E_{BP} determined for the primitive unit cells.

II. Dissemination of Computational Models and Results

The general DFT-based approach uses established methods and available DFT codes to perform the calculations, supported by scripts developed at LLNL for analysis and

problem setup. Published manuscripts describing the results provide sufficient details of the computational parameters to enable researchers skilled in DFT to reproduce the results. A significant volume of data output comprises the relaxed atomic structures for the materials and defects studied. Data files for these structures will be made available on a publically accessible website hosted at LLNL and/or mentioned in Supplementary Material accompanying the publications and available by request. Analysis scripts related to the methodologies also may be requested.

In addition, teaching and training of the application of the methods used, in particular toward computation of the relevant parameters for the problem at-hand as described throughout this report, was accomplished by supporting graduate student trainees through the Computational Chemistry and Materials Science (CCMS) Summer Institute at LLNL (http://www.llnl.gov/ccms/). The CCMS is an annual summer program that hosts about 10-15 graduate students for 10 weeks to work with a mentor on a specific project involving computational chemistry or materials science. Students experience a mix of lecture-type training on state-of-the-art methods as well as hands on experience using LLNL high-performance computing resources to address problems of relevance. This project directly supported one student, Aakash Kumar, for CCMS 2015, during which he worked on DFT modeling of copper-sulfide materials and also sensitivity analysis of SCAPS device models. Several other students in recent years have also been trained in related methods, supported by LLNL institutional funds or other projects.

III. Experimental Methods

All experiments used materials produced on production tools at MiaSolé High-Tech LLC in San Jose, California. Process conditions were varied slightly to study the effects of selected process variables on device microstructure, microchemistry, and performance. All process variables except as noted in this report were kept constant under their process of record conditions.

All layers that comprise MiaSolé's solar cell are deposited sequentially onto a flexible stainless steel substrate in a single pass in an all-PVD process system. One difference of this approach compared to most other manufacturing methods is the replacement of the chemical bath deposited CdS layer with a PVD CdS deposition. Samples studied here were all processed in MiaSolé's production equipment using process settings similar to manufacturing settings.

For comparison with conventional CBD CdS methods, stainless steel samples, coated up to the CIGS absorber step identically to those with PVD-CdS, were removed from the deposition tool and coated with CdS by CBD. The CBD process was performed in an aqueous solution of $CdSO_4$, NH_2CSNH_2, and NH_4OH, at a temperature of 65 °C for 16 min. The samples were rinsed in water, dried, and finished with a ZnO deposition sequence following a process similar to that used for the PVD samples. Every effort was made to ensure that the samples with CBD-CdS were as nearly identical to those with PVD-CdS as possible.

The performance of the photovoltaic devices studied in this project is given in **Table II**. These devices are 109.2 cm^2 interconnected cells produced from specific variations around the MiaSolé process of record (POR) of an 8th generation production process

circa 2013. The analysis of these samples represented the majority of the project effort. Other samples analyzed but not included in this table were not fabricated into interconnected devices and are discussed below where results are described. While the specific devices studied were fabricated with a previous generation production process, the knowledge gained regarding improvements in buffer material are expected to apply as well to current generation devices, which have not significantly modified the buffer process compared to the earlier generation.

Table II. MiaSolé Samples Studied in this Project

(a) 8th Generation Experimental Samples sent October 2013:

Experiment	ID	Eff.	Jsc	FF	Voc
Process of record	SBR4680-G01	14.8	32.08	0.66	0.68
CdS higher O	SBR4680-G02	15.0	32.67	0.68	0.67
CdS lower O	SBR4680-G09	13.8	31.68	0.64	0.67

(b) 8th Generation Experimental Samples sent April 2014:

Experiment	ID	Eff.	Jsc	FF	Voc
High oxidation	SBR4964-G19	9.0	30.37	0.49	0.61
Extreme low oxidation	SBR4964-G20	13.4	31.08	0.73	0.58
No oxidation	SBR4964-G21	11.5	30.08	0.70	0.54
Process of record	SBR4964-G25	15.9	31.81	0.74	0.67

All the TEM samples were prepared by a lift-out technique in an FEI Focused Ion Beam instrument (Helios Nano Lab 600i). A low voltage and small current of the Ga ion beam (1 kV, 8 *p*A) was used to clean the surface damage and remove any Ga ion beam implantation following the higher voltage and current ion beam milling step used to produce the sample. The samples were stored in a dedicated TEM sample preservation capsule that is filled with dry N_2 to protect from gradual oxidation. Before being loaded into the TEM, the samples were further cleaned using a Fischione Model 1040 NanoMill specimen preparation system to further minimize the Ga-induced surface amorphous layer and other damage. The TEM sample was tilted to a [021] CIGS zone axis where clear high resolution images of the interface were obtained without any indication of overlap of the CdS and CIGS. Note that in these samples typically the CdS grows epitaxially on the CIGS so a lattice image of the CIGS also provides a lattice image of the CdS. STEM-EDS maps were acquired in a FEI Titan TEM operating at 200kV at the National Center for Electron Microscopy, Molecular Foundry, Lawrence Berkeley National Lab. The EDS detector is a Super-X quad windowless detector with a collection solid angle of 0.7 steradian enabling elemental mapping, typically in several minutes. The atomic resolution STEM-high angle annular dark field images were

collected in a probe-aberration-corrected JEM ARM 200CF at the University of Illinois at Chicago. The inner and outer acceptance angles were estimated to be 68 mrad and 280 mrad, respectively. EDS line profiles were constructed from areas selected from the lattice images so that composition and microstructure could be matched. Energy filtered images were obtained at the University of Illinois in a JEOL 2010F instrument.

To demonstrate that the results are not related to the FIB sample preparation technique, some samples were prepared by traditional methods in which the samples were glued to thicker substrates and face-to-face, sectioned by sawing, and then thinned by grinding and polishing. Final preparation was by low energy, low angle Ar ion milling at 77K in a Gatan ion miller.

Secondary ion mass spectrometry (SIMS) measurements were performed in two instruments, a Cameca IMS-5f conventional SIMS instrument and in a PHI TRIFT III time of flight instrument. The results reported here are for the Cameca but similar data was obtained using the TRIFT III with better mass resolution, all masses recorded, but lower signal-to-noise. The Cameca measurements were taken in positive secondary ion mode using a Cs^+ primary beam. The Cameca data shows mass interferences between some signals such as O_2 and S, Zn and S_2. These were corrected based on comparison to the TRIFT III data as follows. The 32AMU signal consisted of 60% S and 40% O signal. The 155 AMU signal (Cs+S) included 4% Cs+O2. Therefore the 155 AMU signal was taken to represent primarily S and was used to remove the S contribution from the 32 AMU signal to yield an O profile. The resulting 32 AMU signal was used to remove the minor component of O contribution to the 155 AMU signal to yield a corrected S profile. The 155 AMU signal was also used to remove 20% of the 64 AMU that apparently resulted from S_2, yielding the Zn profile. A rolling five point average was used to further reduce noise in all of the profiles. The resulting profiles were consistent with the TRIFT III data but with improved signal-to-noise.

Computational Results for T-1

T-1 Calculate properties of intrinsic defects and impurities in bulk CdS

ST-1.1: Build atomistic models of CdS containing intrinsic defects

ST-1.2: Calculate formation energies of each defect as function of Fermi level to determine relative concentrations and electronic character

ST-1.3: Repeat calculations for impurities

M(T-1): Report on theoretical electronic nature of defects in bulk CdS

The original scope of this task focused solely on bulk CdS and calculations using standard density functional theory (DFT), to provide baseline results for the electronic properties of native defects and common impurities in this benchmark buffer layer material. However, due to the availability of increased computational resources, we were able to perform all analyses at the screened hybrid functional (beyond-DFT) level, which is computationally much more demanding than standard DFT but also greatly improves the description of semiconductor band gaps and the defect states within them. We completed the planned calculations for all native defects (vacancies, antisites, interstitials, and a number of vacancy complexes: nominally about a dozen defects,

although each one involves calculations of a number of symmetry configurations and charge states). The known important bulk impurities O, H, and OH were completed (about 7–12 configurations each). A few configurations of C and N impurities were also completed. We also considered a large number of complexes of impurities with each other (e.g. O–C, N–H) and with native vacancies to establish the lowest energy configurations and find a number of complexes are stable and relevant defects. Detailed results are described below.

In addition, all calculations for bulk CdS were also performed for bulk ZnS, which is a justified expansion of scope of T-1. By performing calculations on ZnS early, we were able to glean important insights into the electronic properties of defects in wide gap materials compared to CdS, particularly related to the absolute positions of the band edges. Our results identified that the substitution of Cd with Zn has the primary effect of shifting the conduction band up by 1.4 eV on an absolute energy scale (decreasing the electron affinity), but does not affect the position of many important gap states, especially the acceptors. Perhaps more desirable would be to shift the valence band downward to open the gap relative to CdS, as with the case of ZnO. Our results confirm this and establish Zn(O,S) alloys as a proming alternative buffer to CdS due to the larger band gap and similarly favorable band edge alignment with CIGS as we describe in more detail below.

The milestone M(T-1) was fulfilled by the publication of the manuscript “Electrical Properties of Point Defects in CdS and ZnS” in *Applied Physics Letters*.[31] Subsequent manuscripts were also published in Refs. 32 and 33 that included an analysis of metastability of defects and a more comprehensive analysis of defect complexes, calculated diffusion barriers, and optical signatures of defects. While nominally analysis of these defect properties in bulk CdS is part of T-1, the inclusion of ZnS and the relevance of diffusion and intermixing impurities to the properties of the CIGS/buffer layer interface actually makes this effort cross-cut T-1, T-2, T-6, and T-7.

Native defects and their influence on buffer properties

We find the qualitative behavior of native point defects to be similar in both CdS and ZnS: the dominant native donors are V_S and cation interstitials (Cd_i, Zn_i), while the dominant native acceptors are cation vacancies. The cation antisite defects (Cd_S, Zn_S) are also donors, but are less favorable. In general we find the formation energies to be high in the *n*-type conditions common to the buffer layers, and thus most native defects will occur in low concentrations that may be difficult to detect. The exception is cation vacancies, which are found to be favorable compensating acceptors in *n*-type buffer layers and occur in much higher concentrations in ZnS than in CdS.

In general, we find that vacancies are the most prevalent defects for *n*-type buffer material, particularly for the cation-rich/S-poor limits summarized in Figure 2. We find that V_S are deep double donors with the ε(+2/0) transition from the +2 to 0 charge states falling 1.72 eV above the VBM for CdS and 2.06 eV above the VBM for ZnS (see Figure 2). The calculated transition levels indicate that V_S will not lead to Fermi levels near the conduction band minimum, and thus are not the source of the commonly observed *n*-type conductivity in CdS buffer layers. However, based on their formation energies, V_S likely act as significant hole-compensating centers for *p*-type CdS or ZnS, pinning the

Fermi level at least 1 eV above the VBM for cation-rich conditions shown in Figure 2(a) and (c). The role of V_S in *n*-type conditions is less relevant due to their low equilibrium concentrations, particularly in the S-rich growth conditions shown in Figure 2(b) and (d).

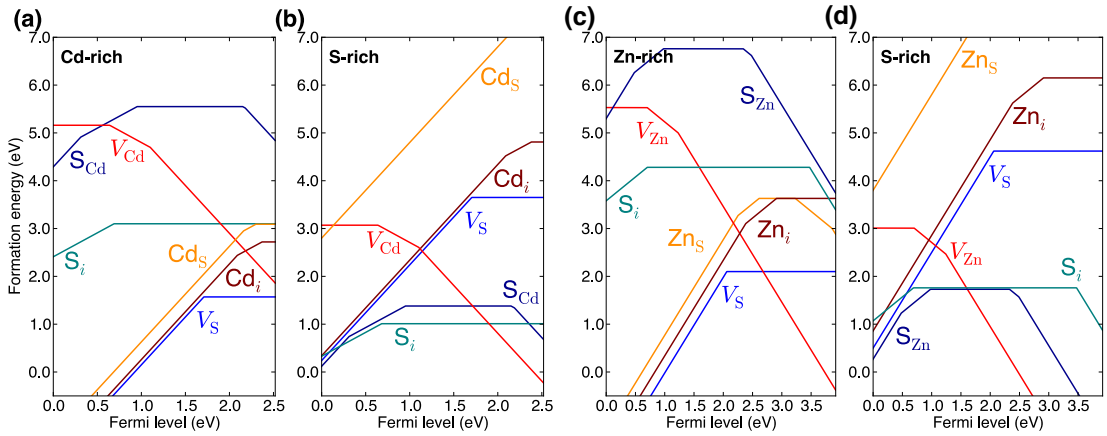

Figure 2. Formation energies of native defects in CdS shown for (a) Cd-rich and (b) S-rich (Cd-poor) conditions. Analogous formation energies for native defects in ZnS, a wider-bandgap alternative buffer candidate, are included (c) for Zn-rich and (d) S-rich (Zn-poor) conditions. Only the most stable charge states are shown for each defect. The Fermi level is referenced to the VBM and ranges over the band gap to the CBM.

Cation vacancies are found to be deep acceptors that can trap up to 2 electrons in the dangling bonds of the adjacent S atoms. The ε(−/2−) transition for V_{Cd} is 1.10 eV above the VBM of CdS, while the analogous level for V_{Zn} is 1.24 eV above the VBM of ZnS. Experimental comparisons are lacking for CdS, but we find the V_{Zn} transition levels in good agreement with experimental data from EPR and ODMR measurements: the latter falling 1.1-1.25 eV above the VBM of ZnS.[34,35]

It is worth noting that the defect charge-state transition levels are similar in the two materials when referenced to their respective VBMs, but that the much larger band gap of ZnS shifts the formation energies near the CBM, since most of the gap opening occurs at the CBM, which we discuss later. This results in very favorable formation energies for V_{Zn}^{-2} in *n*-type ZnS, particularly for S-rich growth conditions. Therefore V_{Zn}^{-2} acceptors will result in significant compensation of ionized donors in *n*-type ZnS. Indeed, this is supported by the relative difficulty in achieving optimal donor ionization efficiencies in *n*-type ZnS and by the extensive literature on *A*-center defects in ZnS, i.e. a complex formed between a V_{Zn}^{-2} and an incorporated donor which we discuss more below.[34] Analogous *A*-centers are also well characterized in CdS and have been implicated for self-compensation in more S-rich conditions,[36] compatible with our results as they are derived from cation vacancies.

Growth-Related Impurities

We also explore the role of common impurities such as H, O, and some of their complexes with native impurities and each other (i.e., OH), as well as C and N impurities incorporated into the buffers via common growth techniques such as CBD and ILGAR methods. The formation energies are plotted in Figure 3 for OH-related

defects in CdS and ZnS**.** We find that interstitial H (H_i) behaves as an amphoteric impurity in both CdS and ZnS, acting predominantly as either a shallow donor or a deep acceptor depending on the position of the Fermi level within the band gap. Interestingly we find the ε(+/−) transition very close to the CBM for CdS, indicating that H_i will act predominantly as a donor in CdS and may pin the Fermi level near the CBM. The transition is much deeper in ZnS, 2.54 eV above the VBM, suggesting further why *n*-type conductivity is more readily achieved in CdS than in ZnS.

Hydrogen can also incorporate on the S site as a shallow donor (H_S), or form an *A*-center when complexed with the cation vacancies. Unlike in ZnO,[37] we find H_S does not form a multi-center bond but instead moves off-site to preferentially bond to individual cations, which is likely a consequence of the larger bond lengths in the sulfides. As an *A*-center, we find that H binds strongly to a S dangling bond within the cation vacancy, which can Coulombically attract up to 2 H. We label these complexes as H_{Cd} and H_{Zn} for brevity, and find their ε(0/−) transition levels 0.59 eV above the VBM for CdS and 0.69 eV above the VBM for ZnS. The cation vacancies passivated by 2 H, which we label as $2H_{Cd}$ and $2H_{Zn}$ in Figue 3, form a neutral complex and are electrically inactive.

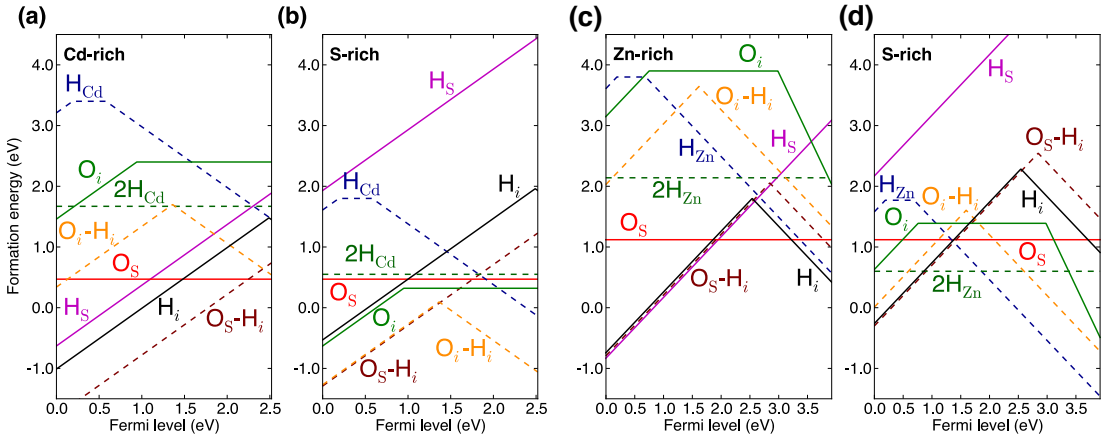

Figure 3. Formation energies of O and H impurities and favorable complexes in CdS shown for (a) Cd-rich and (b) S-rich (Cd-poor) conditions. Analogous formation energies for native defects in ZnS are included in (c) for Zn-rich and (d) S-rich (Zn-poor) conditions. Only the most stable charge states are shown for each defect. The Fermi level is referenced to the VBM and ranges over the band gap to the CBM.

The binding energy, defined as the difference in formation energies between the complex and the isolated constituents, is 1.90 eV for the first H to bind the the V_{Cd}^{-2} in CdS and form H_{Cd}^{-}. The binding of the second H gains an additional 1.31 eV relative to the H_{Cd}^{-} and H_i^{+} to form $2H_{Cd}^{0}$, a binding energy large enough to overcome entropic limitations to the formation of such complexes.[25] The analogous binding energies are even stronger in ZnS at 2.23 eV and 1.61 eV to bind the first and second H to the V_{Zn}^{-2}, respectively. The large binding energies of these complexes suggest that the intentional incorporation of H_i under controlled conditions may help fully passivate compensating centers like isolated cation vacancies or *A*-centers and enhance the efficiency of *n*-type doping in ZnS and CdS.

Next we consider C and N impurities in the buffer, where we find the isolated impurities can lead to distinct electrical behavior depending on the growth conditions (see Figure 4). For CdS in the Cd-poor (S-rich) limit, C most favorably incorporates on Cd site (C_{Cd}) in *n*-type conditions, acting as a donor. In the Cd-rich limit, we find isolated C incorporates on the S site (C_S) and acts as a compensating double acceptor in *n*-type conditions. The ε(–/–2) of C_S is 0.15 eV below the CBM of CdS, which we predict falls very close to the CBM of more In-rich CIGS, thereby acting as a possible electron trap. As an interstitial, we find C_i is only favorable for Fermi levels near mid-gap and below, far from *n*-type conditions, indicating that C is not expected to incorporate interstitially in CdS. Furthermore, while our formation energies are an upper bound representing the limit of thermodynamic equilibrium, the energies are high and suggest that isolated C impurities are not readily soluble in CdS buffer layers. The results are similar for ZnS, but the formation energy of C_S is also much lower in *n*-type ZnS than for any of the C-related defects in *n*-type CdS, particularly for the Zn-rich (S-poor) conditions.

We previously found that cation-rich conditions are recommended to minimize recombination centers and compensation stemming from cation vacancies in ZnS and CdS. In these same conditions, we find C impurities are far more likely to be incorporated into ZnS buffers, limiting overall device efficiency through possible recombination and compensation effects. These results suggest that the electrical properties of ZnS buffers likely suffer more from growth processes employing C-containing precursors than does CdS.

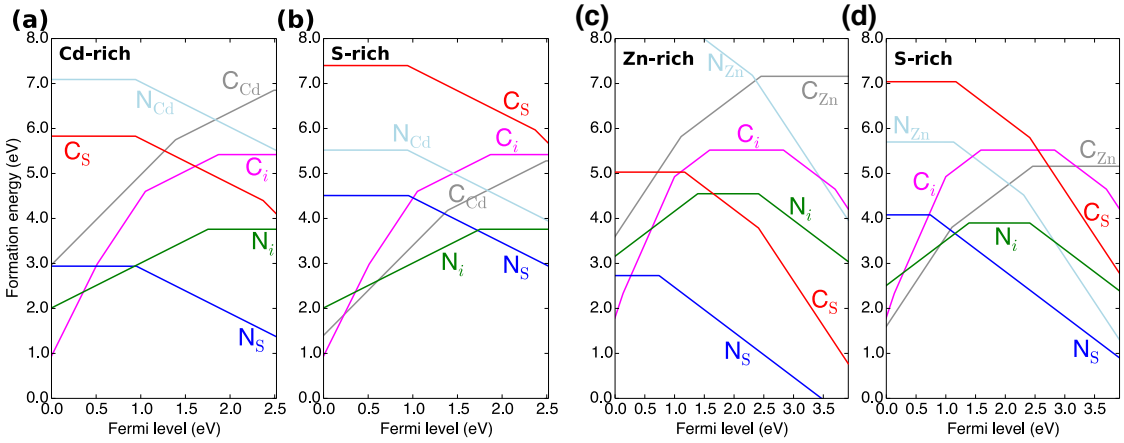

Figure 4. Formation energies of C and N impurities in CdS shown for (a) Cd-rich and (b) S-rich (Cd-poor) conditions. Analogous formation energies for native defects in ZnS are included in (c) for Zn-rich and (d) S-rich (Zn-poor) conditions. Only the most stable charge states are shown for each defect. The Fermi level is referenced to the VBM and ranges over the band gap to the CBM.

From Figure 4 we also predict N impurities to be much more readily incorporated than C in CdS and ZnS. We find isolated N always prefers to incorporate on the anion site (N_S) relative to the cation site (N_{Cd}, N_{Zn}), acting as a deep acceptor. For CdS, this in contrast to C that can favorably occupy both sites depending on the chemical conditions. On the S site, N_S exhibits a ε(0/–) transition level 0.95 eV above the VBM in CdS and 0.73 eV in ZnS, which identifies it as a deep acceptor with its trap state located well below the

VBM of CIGS**.** When incorporated as a split-interstitial, N_i is a deep donor in CdS and ZnS. An acceptor form of N_i is also stable for Fermi levels above ~2.4 eV from the VBM, making N_i amphoteric in ZnS, but not in CdS due to the smaller band gap. In CdS, N_i remains electrically neutral in *n*-type conditions. From the formation energies in Figure 4, it can be seen that N_i is nearly always higher in energy than N_S in both materials, particular for *n*-type conditions, thus isolated N is predicted to readily incorporate on the S site in *n*-type material and compensate the conductivity in both CdS and ZnS.

We also investigated the interaction of H_i with C and N impurities and include the formation energies of several complexes Figure 5. The hydrogenation of the C and H impurities is found to significantly lower the formation energy of the isolated C and N, potentially enhancing their concentrations in the buffer layer. Annealing steps can lead to the breaking of these complexes and activation of isolated C and N, which we find to be most stable as defects with deep levels (i.e. N_S and C_S) that may contribute to carrier recombination and device metastabilities. To characterize the stability of these complexes, we calculated their binding energies, defined as the energy difference between the isolated constituents and the complex.

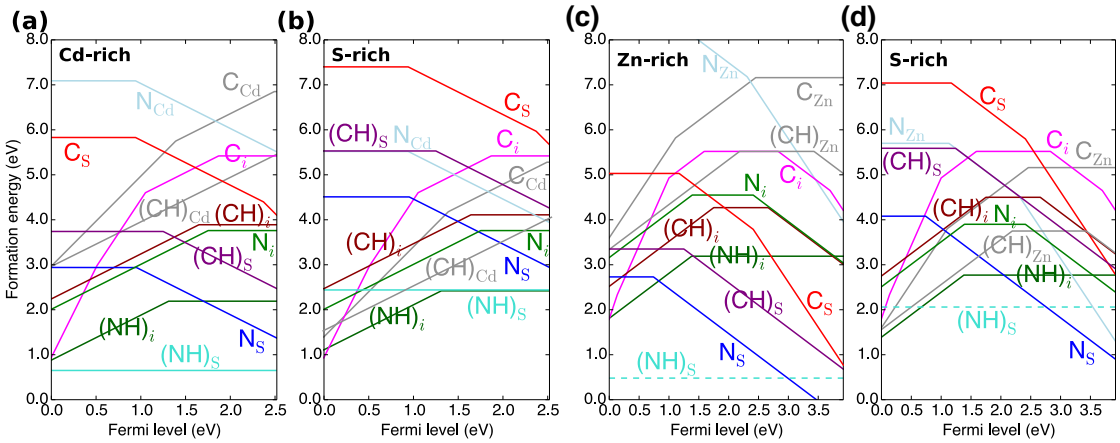

Figure 5. Formation energies of C-H and N-H complexes in CdS shown for (a) Cd-rich and (b) S-rich conditions. Analogous formation energies for native defects in ZnS are included in (c) for Zn-rich and (d) S-rich (Zn-poor) conditions. Only the most stable charge states are shown for each defect. The formation energies from Figure 4 are included for comparison.

Of the complexes in 5 we find the neutral $(NH)_S$ complex formed between H_i^+ and the deep acceptor N_S^- to be generally the most favorable. Thus in environments in which both N and H are present, the incorporation of these species into the buffer may be significantly enhanced. The binding energies are large and nearly identical in both materials: 2.23 eV in CdS and 2.24 eV in ZnS, suggesting the complexes are thermally stable below temperatures ~440 °C. The complexing of H_i^+ and the N_S^- removes the trap state of N_S from the band gap, thus H_i^+ may effectively and advantageously passivate isolated N impurities that may have been incorporated in CdS and ZnS unintentionally.

The C-H complexes are also more favorable than the isolated C and H species. In *n*-type and cation-rich conditions, the most favorable complex is $(CH)_S$, which acts as a

deep acceptor. Unlike the $(NH)_S$ complex, $(CH)_S$ maintains localized states in the band gap that may continue to act as traps in both CdS and ZnS. The ε(0/–) transition level falls 1.35 eV above the VBM for CdS and 1.24 eV for ZnS, so $(CH)_S$ will act as compensating acceptors for Fermi levels near the CBM. From these considerations, growth methods and environments that are rich in C and H may lead to impaired device performance due to an increased concentration of traps in the buffer.

Defects and Optical Metastability

In Figure 6 we show the configuration coordinate diagrams describing the optical transitions between the conduction band and the sulfur vacancy (V_S) in CdS and ZnS. From this analysis we characterize the absorption and emission energies resulting from the possible transitions to and from the localized defect states. The transitions shown in Figure 6 are relevant for *n*-type buffers and "red-light" conditions where the excitation energies are less than the band gap of the buffer, i.e. the electrons are exchanged with unoccupied states in the conduction band rather than the valence band. These excitations may limit device performance by reducing the incident photon flux on the absorber and the occupation of trap states in the device, which changes the effective concentration of recombination centers. These optically-induced changes in defect charge states associated with large configurational changes can lead to metastabilities in devices under light soaking.

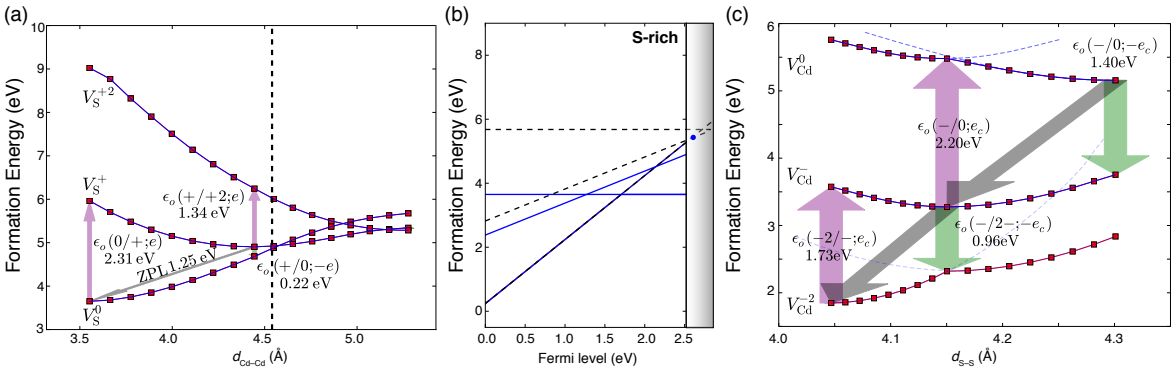

Figure 6. Configuration coordinate diagrams showing transitions to the conduction band for native vacancies in CdS. (a) For V_S the configuration coordinate is plotted as the average cation-cation distance of the cations surrounding the vacancy (d_{Cd-Cd}). (b) Formation energies for V_S in for all charge states in their relaxed geometries (solid blue lines) and when assuming the relaxed geometry of the fully ionized V_S^{2+} (dotted black lines). The location of transition levels above the conduction minimum for CdS is indicative of persistent photoconductivity due to V_S. (c) For V_{Cd} the configuration coordinate is plotted as the average S–S distance surrounding the vacancy (d_{S-S}). The absorption energies ~2 eV to affect the V_{Cd} recombination centers may contribute to the "red-kink" metastability observed in some CIGSe-CdS devices.

Focusing on CdS, we find that the (0/+) optical transition for V_S occurs in the visible range at 2.31 eV, and the subsequent (+/2+) excitation occurs in the infrared at 1.34 eV. From Figure 6(a) and (b) it can be seen that the transition energy to return the V_S^{2+} to V_S^{+} is above the CBM, indicating that a barrier exists to recapture the photo-excited electron into the localized states associated with the V_S. This is a signature of persistent

photoconductivity (PPC),[38] which we find in CdS but not in ZnS. In Figure 6(c) we show the transitions associated with the V_{Cd}, which we previously showed is likely the dominant native defect and recombination center in CdS buffers. We find that 1.73 eV is required to excite the (2–/–) transition, and 2.20 eV for the subsequent excitation of (–/0). The former energy is compatible with the "red-kink" effect, a well-known metastability observed in the *I-V* characteristics of certain CIGSe/CdS based devices under red illumination (~2 eV). We also investigated the absorption energies associated with A-centers (discussed later) and identified a range of absorption energies within the range that is typically associated with the red-kink effect. Due to the possibility of high concentrations of V_{Cd}^{-2} in *n*-type CdS buffers, we believe that these optical transitions may contribute to the loss of photocurrent observed in the red-kink regime.

Computational Results for T-2

T-2: Calculate properties of CdS/CIGS interface

ST-2.1: Construct CdS/CIGS interface models

ST-2.2: Calculate electronic structure of interface defect states

[ST-2.3: Determine effective barrier height and Fermi-level pinning characteristics of interface from electronic structure

Details of the absorber buffer interface are critical to understanding photovoltaic performance. The band alignment between the absorber and buffer layers has been shown to have a large influence on the interfacial charge and the resulting device performance. For example, we include our calculated band alignment for the absorber, buffer, and window layers in Figure 7, where we identify the small spike-type offset between the CIGS-CdS conduction bands known to facilitate good performance. Additionally, the presence of interfacial defects or dopants can also impact transport by creating recombination centers that may significantly deplete photocurrent or creating trapped charges that can affect band bending. In Figure 7 we also include the deep levels associated with all of the native defects considered in T-1, which illustrates the possibility for active recombination centers from native defects like cation vacancies.

For this task, the electronic properties of the interface between the absorber and the buffer are studied. This involves a number of models: (i) intermixing may occur at the interface, injecting impurities into each material from the adjoining material; (ii) inter*phases* may form chemically between the adjoining materials, altering the local electronic properties such as band alignments; (iii) electronic states may arise from imperfect bonding at material interfaces (absorber/buffer or grain boundaries); and (iv) electronic states may arise from (or be passivated by) impurities at material interfaces.

Here, we will describe primarily the affects of intermixing impurities, in terms of their electronic properties and an assessment of their diffusion rates. We consider the constituent elements of the absorber, as well as Na and K, which may be intentionally incorporated during fabrication. Our results strongly complement the experimentally obtained distributions of such impurities in real devices as part of T-4. The properties of possible interphase materials, such as Cu_2S are also discussed.

Interfacial Intermixing-Related Impurities

To assess the role of interdiffusion at the absorber-buffer interface, we show in Figure 8(a) and (b) the formation energies of Se, Ga, and In defects in CdS and ZnS (shown for cation-rich conditions). The formation energies show that Se is readily incorporated on the S site in CdS and ZnS, supporting the case for (S,Se) anion intermixing at the buffer-CIGS interface.[36,39,40] However, we find that as an isolated impurity, Se_S does not lead to any significant effects on the electronic structure, acting as a neutral defect with all associated states resonant within the valence and conduction bands. Substitutional Ga_{Cd} and In_{Cd} act as shallow donors in CdS, whereas their analogs in ZnS exhibit deeper transition levels but still act predominantly as donors for Fermi levels ranging over the band gap. As interstitials they are also donors, indicating that Ga and In intermixing into the buffer dopes the interface and can influence the overall band bending. In both materials we find that the formation energies of the group-III impurities on the buffer cation site increase down the group, suggesting that more Ga-rich CIGSe may experience more intermixing at the interface.

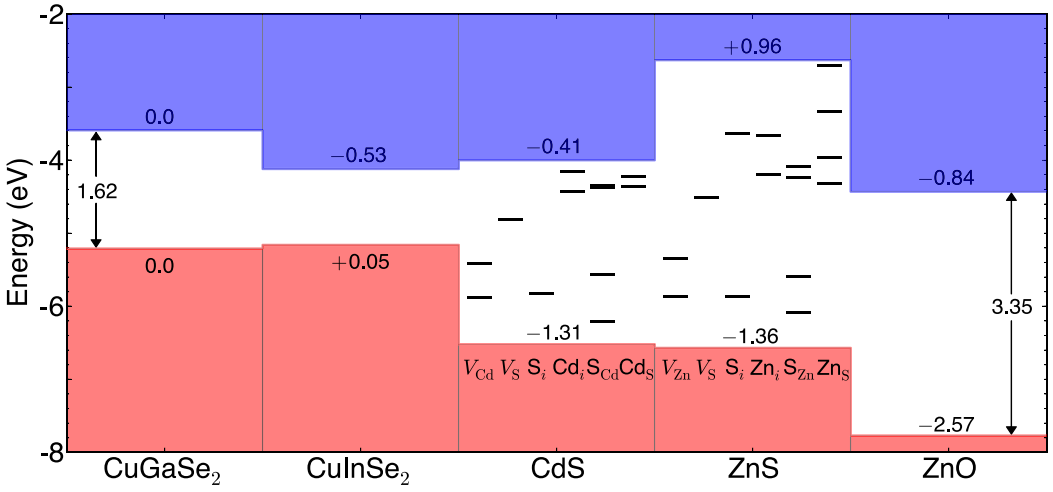

Figure 7. Diagram of the band line-ups for the bulk materials comprising an ideal CIGSe-based thin-film solar cell as aligned via the charge neutrality level. Numbers indicate the relative offsets, in eV, compared to CGSe. The lines within the band gap of CdS and ZnS represent the positions of thermodynamic transition levels of the native defects.

The diffusion of the favored substitutional impurities into the buffer beyond the interface may proceed via vacancy-assisted or interstitial migration. To address the former, we calculated the migration barriers for native cation vacancies in the buffers, while for the latter we calculated the barriers for In_i^{+}, Ga_i^{+}, and Se_i^{0} interstitial migration paths. We used the nudged elastic band method with the HSE06 hybrid functional to compute all barriers. The calculated diffusion barriers are summarized in **Table III**, for both in-plane and out-of-plane directions in the wurtzite lattice relative to the crystallographic *c* axis. We find that the migration barriers of the cation vacancies are largely isotropic, 1.02 eV (1.02 eV) for V_{Cd}^{-2} in CdS and 1.21 eV (1.23 eV) V_{Zn}^{-2} in ZnS in paths parallel (perpendicular) to the *c*-axis of the wurtzite lattice. These barriers are low enough to facilitate cation vacancy migration at temperatures as low as ~100 °C. Estimating the

activation energy (E_a) as the sum of the formation energy and migration barrier, we find that diffusion of Ga and In defects into the buffer bulk are more likely to proceed via vacancy-assisted rather than interstitial-mediated migration.

Table III. The calculated migration energy barriers in eV, parallel to (|| *c*) and perpendicular to (⊥ *c*) the wurtzite *c*-axis, for various defects stable in *n*-type CdS and ZnS.

	CdS - wurtzite		ZnS - wurtzite	
	|| *c* (eV)	⊥ *c* (eV)	|| *c* (eV)	⊥ *c* (eV)
V_M^{2-}	1.02	1.02	1.21	1.23
In_i^+	0.73	0.51	0.66	0.38
Ga_i^+	0.94	0.75	0.95	0.91
Se_i^0	0.38	0.40	0.47	0.42
Cu_i^+	0.64	0.26	0.30	0.23
Na_i^+	0.99	1.09	1.51	1.82
K_i^+	1.51	0.50	1.49	0.45

Next we turn to Cu-related defects, shown in Figure 8(c) and (d). In *n*-type conditions we find Cu most favorably acts as a deep acceptor when substituting on the cation site, exhibiting nearly the same transition level ~1.25 eV above the VBM in both CdS and ZnS, in good agreement with reported experimental values of 1.1–1.25 eV.[35] Even for the cation-rich conditions in Figure 8, the formation energies of Cu_{Cd} and Cu_{Zn} are low for *n*-type material, where Cu effectively leads to Fermi-level pinning at least 0.65 eV below the CBM in ZnS. We find that as an interstitial, Cu_i acts nearly exclusively as a donor Cu_i^+ in CdS and ZnS. In terms of their absolute formation energies, Cu_i^+ are significantly more likely to occur in CdS than in ZnS *n*-type buffer layers. The migration barriers for Cu_i^+ are also the lowest of any of the CIGSe-related defects in both materials (**Table III**). From the approximate 1.87 eV E_a for Cu_i^+ diffusion in CdS, we predict the incorporation of Cu into CdS is more likely than in ZnS, and is estimated to occur for processing conditions above ~400°C. The attraction between mobile Cu_i^+ and Cu_{Cd}^- may act as a driving force for Cu clustering that can facilitate the formation of Cu-rich phases, which we observe experimentally.

We also include Na and K-related defects also in Figure 8(c) and (d) which we find to exhibit the same qualitative behavior as Cu. Na and K have been shown to improve the performance of CIGS-based cells when incorporated into the CIGS either intentionally[41] or unintentionally,[42] but their interaction with the buffer is not currently understood. Even in CIGS the exact origin(s) of these improvements are not known, but it was recently suggested that Na may limit the diffusion of Cu in the CISe,[43] having implications in the reduction of Cu-deficiencies at the interface. Like copper, Na and K are most favorably incorporated on the cation site for *n*-type conditions, where they act as compensating acceptors. Substitutions on the S site and interstitials also act predominantly as donors

in both CdS and ZnS, with K_i and Na_i always more preferable to S substitution. Due to the similar behavior of Cu, Na, and K in the buffer, it follows that the incorporation of alkali impurities can make up for the lack of Cu typically present at the absorber-buffer interface and lead to a partial passivation of recombination centers stemming from acceptors like cation vacancies, a result consistent with the increase in open-circuit voltage typically associated with Na incorporation.[44] However, this must be balanced against the intention to inversion dope a Cu-deficient absorber surface with Cd donors from the buffer layer.

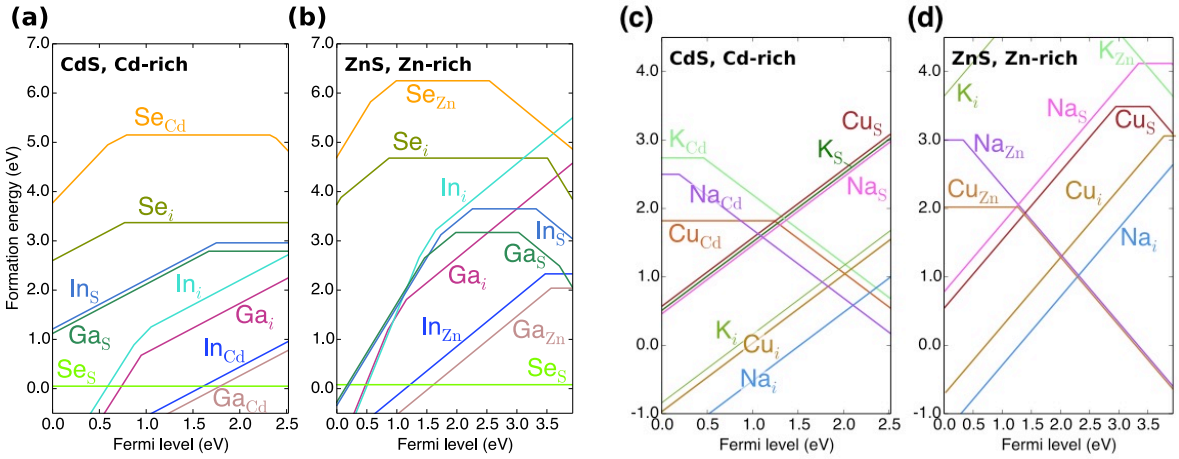

Figure 8. Formation energies in of Se, In, and Ga defects in cation-rich conditions shown for (a) CdS and (b) ZnS. Formation energies of Cu, Na, and K defects in cation-rich conditions shown for (c) CdS and (d) ZnS.

We also investigated the energies and mobilities of Zn and Sn-related defects in the buffers. These elements may be incorporated either from $Cu_2ZnSn(S,Se)_4$ absorbers, or from common window layers like ZnO or SnO_2. The formation energies summarized in Figure 9(a) indicate that thee impurities are likely to act as neutral defects in *n*-type CdS buffers and are not expected to cause recombination losses. However, in Figure 9(b), we include the formation energies of A-centers that result from the complexing of substitutional group-III donors and a cation vacancy acceptor. These defects are found to be favorable and thermodynamically stable, exhibiting binding energies on the order of 1 eV, and are detrimental compensating acceptors in *n*-type buffer material.

Lastly we evaluated both the thermodynamic and optical transition levels associated with the favorable defects in *n*-type buffers to identify which defects may be most problematic for dark and light-induced recombination losses. Our results are included in Figure 10, where we show the positions of the defect levels relative to the band edges. Our results identify that the levels associated with photoexcited V_{Cd}, A-centers, and Cu_{Cd} all are close to the energies most prone to undergo Shockley-Read-Hall recombination, which would lead to photocurrent losses. These results suggest that Cu incorporation into the buffer as isolated impurities is detrimental to performance.

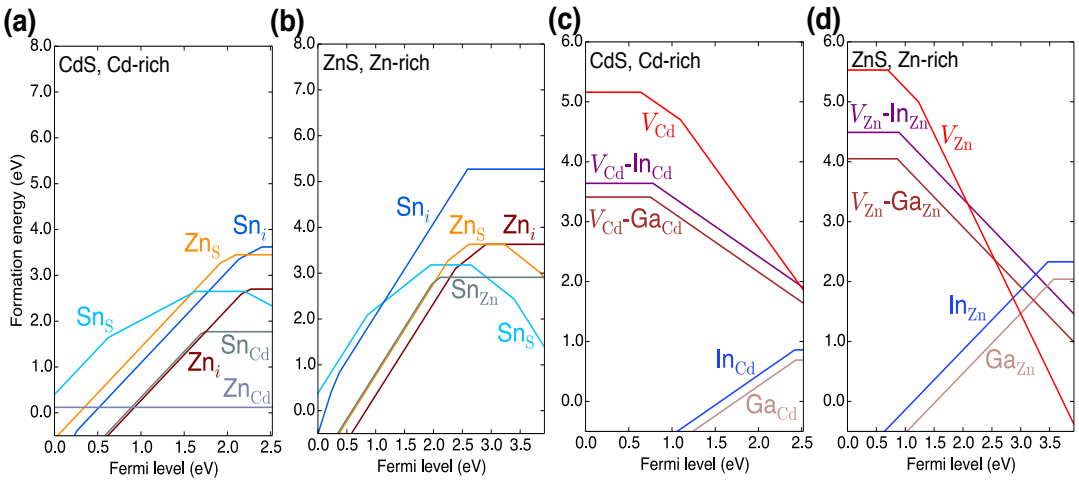

Figure 9. Formation energies of Zn and Sn-related defects in CdS (a) and ZnS (b) shown for cation-rich conditions. These may be relevant for photovoltaic devices employing $Cu_2ZnSn(S,Se)_4$ absorbers and/or ZnO or SnO_2 window layers. Formation energies of A-center defects in CdS (c) and ZnS (d) shown for cation-rich conditions.

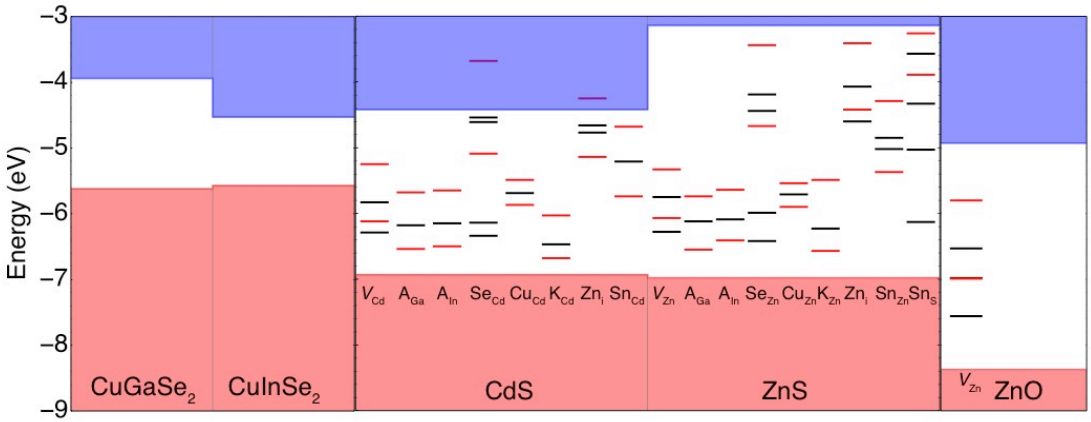

Figure 10. Band lineup of CIGS/(CdS,ZnS)/ZnO taken overlaid with the transition levels of the most stable absorber-related defects with deep levels. The (highest) thermodynamic transition levels are shown in black and the optical transition levels associated with the stable charge state for n-type conditions are shown in red. Grey lines represent the other thermodynamic transition levels, but we do not include their associated optical transition energies as they do not correspond to the energetically preferred charge states in n-type buffers. The dotted black lines represent the intrinsic Fermi levels for each material as determined from the calculated DOS and represent important reference levels for characterizing the rate of Shockley-Read-Hall recombination associated with particular defects in dark and illuminated conditions.

Assessing properties of Cu-rich phases: Cu_2S electronic structure

Our experimental efforts have identified the existence of Cu-rich domains at the buffer-absorber interface in CIGS devices that are consistent with nearly stoichiometric Cu_2S. While the Cu_2S-CdS heterojunction has a long history in thin-film photovoltaics,[45] the exact consequences of these layers in CIGS devices are unknown. Our initial theoretical studies are aimed at establishing the electronic structure for the Cu_2S observed in the TEM images and then determining how sensitive the electronic and optical properties are to stoichiometry and crystal structure.

The theoretical ground-state structure predicted for Cu_2S is a monoclinic phase known as low-chalcocite, but the TEM and diffraction data indicate a cubic modification with a lattice constant of 5.51 Å. In Figure 11 we include the calculated band structure and density of states (DOS) for a cubic form of Cu_2S that adopts the antiflourite structure with a calculated lattice constant of 5.60 Å, in good agreement with the experimental data. Our results on this model structure identify a very low and nearly isotropic effective electron mass of ~0.19m_e and a larger but more anisotropic hole effective mass. For the Γ-X direction, we calculate a hole effective mass of 0.56m_e, which is similar to or even lower than the hole mass reported for CIGSe (0.72m_e).[46] This suggests that Cu_2S layers should be exhibit high mobilities for both carrier types that may facilitate charge transport.

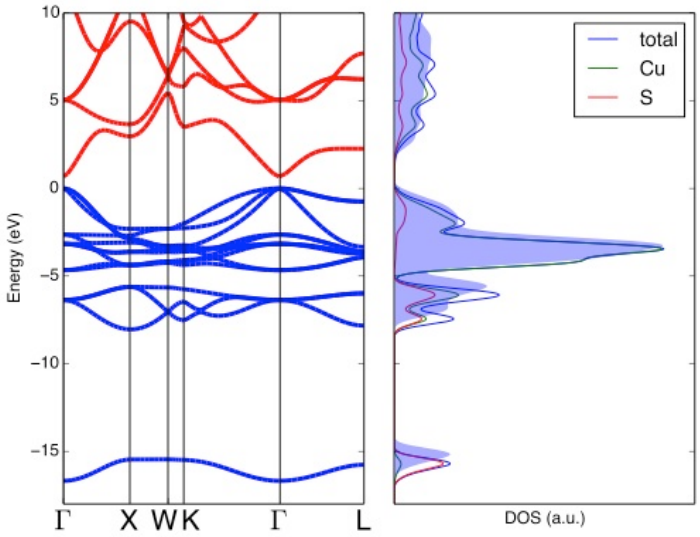

Figure 11. (a) Calculated band structure and density of states for cubic Cu_2S in the antifluorite structure. It is a direct band gap material with a conduction band of Cu *s* orbital character. The density of states of monoclinic Cu_2S (low chalcocite) is included as the shaded blue region and indicates the qualitative electronic structure may be consistent across many of the different Cu_2S structures.

The antiflourite structure for Cu_2S is found to be unstable in its highly-ordered form, and a more realistic structure exhibits partial occupancies of the various lattice sites.[47] We analyzed how the local structure influences the properties of cubic Cu_2S, focusing on how the band gap and band offsets change as function of disorder and stoichiometry. In

Figure 11 we also include the DOS of low chalcocite as an initial representative of disorder in the Cu_2S lattice and identify a notably larger band gap (1.2 eV compared to 0.67 eV) yet qualitative similarities with the ordered antiflourite structure. Previous studies have identified how the disorder influences hybridization that increases the band gap of Cu_2S from the ordered structure,[47] but how this disorder influences the band edges on an absolute energy scale has yet to be determined and would beneficially inform the parameterization of Cu_2S layers for future device model simulations of more realistic CIGSe devices.

Sample Fabrication: Tasks T-3 and T-8

Tasks 3 and 8 are identical for the two portions of the project and are reported together here. Samples will be fabricated throughout the project. The original statement of these tasks specified a number of samples per unit time. This was done at MiaSolé for the project. However, because of the long time necessary to analyze the samples only a small number of samples (described in the experimental section) were studied. These covered a spectrum of process conditions. It was found to be more important to study the samples in detail than to study a larger number of samples.

Experimental Results for T-4 and T-9

Tasks 4 and 9 are identical for the two phases of the project, so results are described together.

- Subtask 4.1 and 9.1: Cross-sectional sample preparation
- Subtask 4.2 and 9.2: Image acquisition
- Subtask 4.3 and 9.3: Device characterization/simulation
- Subtask 4.4 and 9.2: Data analysis
- Milestone T-4: Report nanoscale spatially-resolved compositional analysis of at least 2 representative samples of CdS/CIGS interface

These tasks were performed on all samples. However, the results showed effects related to specific microstructural and microchemical behaviors. Therefore these are described below by type of result (microstructure and microchemistry) and the implications for the behavior of devices. Milestone 4 was satisfied through the publication of a paper entitled “Microstructural and chemical investigation of PVD-CdS/PVD-$CuIn_{1-x}Ga_xSe_2$ heterojunctions: a transmission electron microscopy study” with authors X. Q. He, G. Brown, K. Demirkan, N. Mackie, V. Lordi, and A. Rockett, published in the IEEE Journal of Photovoltaics (2014). The results were described in a presentation at the 2014 IEEE Photovoltaic Specialists Conference with further details presented at the following conference in 2015.

Microstructure of the Heterojunction

A series of TEM measurements were performed to understand the nanochemistry and nanostructure of the heterojunction area of the devices. No detailed microanalysis of other portions of the device was carried out to protect the intellectual property of MiaSolé.

Figure 12 shows a typical high resolution TEM image from the CIGS/CdS heterointerface taken along the CIGS [021] zone axis. The CdS layer displays a uniform coverage on the CIGS surface with a thickness of ~30 nm. The diagonal dark band in the upper right side of the image was found to mark the CIGS/CdS boundary and the diagonal dark band on the lower left marks the CdS/ZnO boundary, as verified by EDS line scans. The nature of the nanochemistry of the interfaces leading to these dark bands is discussed below. Clear lattice images were obtained from the CdS, demonstrating not only crystallinity, but crystal orientations registered to the CIGS. Concurrent lattice images would not otherwise be obtained. The crystallinity of the CdS was determined from the lattice images by fast Fourier transformation (FFT; insets in Figure 12). Due to the small scale of the CdS and domain sizes observed, selected area diffraction patterns were not possible. By indexing of the Fourier transforms we have determined that the epitaxial relationships for the CdS on the CIGS are {0001} CdS || {112} CIGS and $[2\bar{1}\bar{1}0]$ CdS || [021] CIGS for the hexagonal phase and {111} CdS || {112} CIGS; (002) CdS || (200) CIGS and [110] CdS|| [021] CIGS for the cubic phase. This is in accordance with the results reported for the CBD-CdS by T. Nakada.[48] We discuss this relationship in more detail below.

In Figure 12, the solid line indicates a domain boundary between the cubic and hexagonal phases in the CdS. Stacking faults are found in both domains. Evidence for extensive stacking faults is provided by the streaking in the Fourier transform patterns in Figure 12. The faults occur on the close-packed planes, as expected. The co-existence of two phases was also found in CBD-CdS,[14] but the domain size was typically a few nm, much smaller than what we show here (several hundred nms). In the case of CBD-CdS the epitaxy only persisted for at most a few nm rather than throughout the entire layer as observed here. (Most CBD CdS shows no epitaxy.) Due to the similarity of free energy of the cubic and hexagonal phases, there may be competition for which phase will form. The question is decided largely by the growth conditions and the relationship of the two phases to the CIGS surface.

To investigate in detail the relationship between the CdS and CIGS, we give a special focus to the hetero-interface. As shown in Figure 13(a) and (b), the interfaces between the CdS and the CIGS are very sharp and coherent, nearly free of any lattice defects along the interface. This is very different from the observation of Abou-Ras *et al.*[49] where they found a high density of interfacial lattice defects. Close examination reveals that the atomic stacking sequence in the perfect CdS lattice follows the well-known “ABCABC” pattern along the $\{111\}$ close packed planes and “ABAB” along the (0001) planes for cubic phase and hexagonal phase, respectively, see insets in Figure 13(a) and (b). Figure 13(c) and (d) are the corresponding Fourier transforms for the images in Figure 13(a) and (b). The relative orientations of the two lattices are shown by the parallelograms on the Fourier transform patterns. Owing to the very small difference in lattice constant between cubic CdS and CIGS, the {111} and (002) peaks from the CdS coincide with the {112} and (200) peaks from the CIGS, respectively. This similarity also explains the absence of lattice defects at the heterojunction. The lattice constant match is sufficiently close that it permits fully coherent growth of the CdS at these thicknesses.

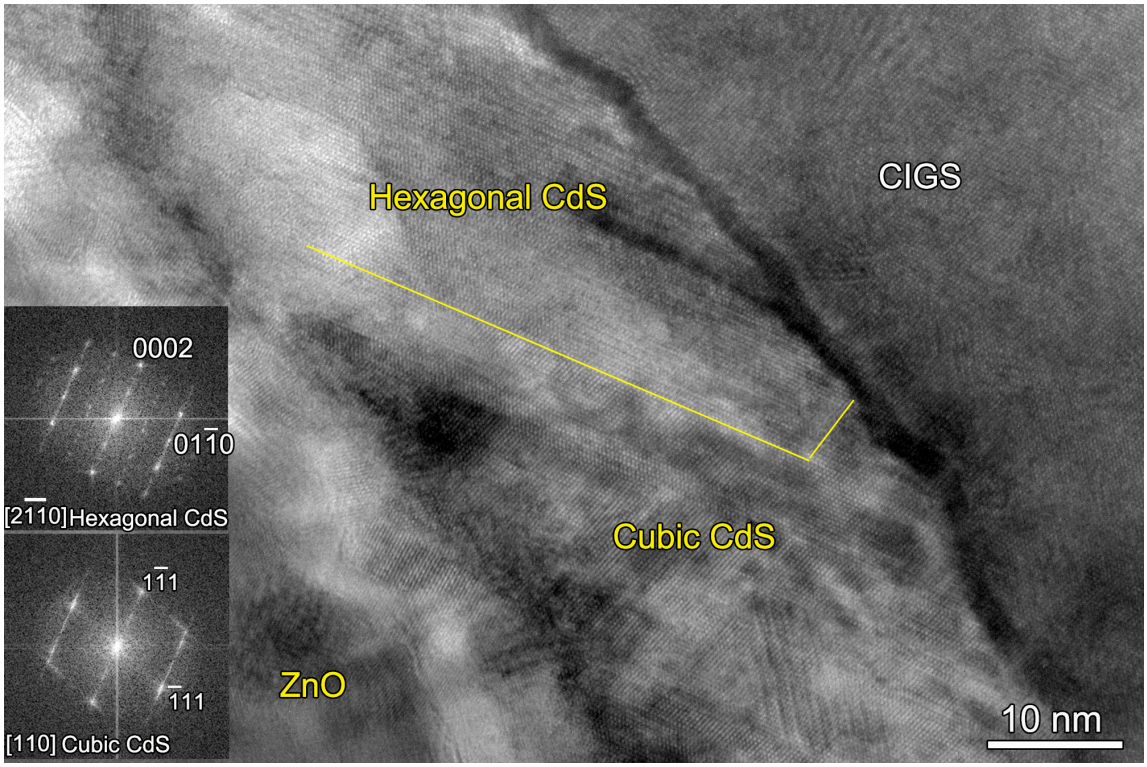

Figure 12. High resolution TEM image showing the coexistence of CdS of cubic phase and hexagonal phase with the corresponding FFT inset. The yellow line marks the domain boundary.

The large CdS domains of pure hexagonal phase are also found in conventional TEM samples. Figure 14 is a typical high resolution TEM image along the hetero-interface. It is shown that well-defined CdS lattice fringes extend through the whole CdS layer despite the stacking faults on the (0001) planes. The inset shows the FFT pattern covering both the CdS and the CIGS, which clearly demonstrates the same epitaxial relationship as that in FIB sample.

More interestingly, the CIGS surface exhibits a regular array of terraces separated by one or two atomic-layer steps along the interface, as indicated by the dashed lines. The average length of a terrace is about 10 nm and the step height between terraces is about 0.7 nm, two interplanar distances of CIGS (112) planes. The interplanar distance of CdS (0002) is very close to that of the CIGS (112) plane. However, there are large lattice mismatches between the other sets of planes, e.g. 0.286 nm for $(200)_{CIGS}$ and 0.316 nm for $(0\bar{1}11)_{CdS}$. That misfit is accommodated by effective rotation of the lattice planes from one material to the other. One can, for example, note $(\bar{1}1\bar{2})$ planes in Figure 14 are inclined with respect to the heterojunction, match nearly exactly with the spacing of the $(0\bar{1}11)_{CdS}$ planes, but are rotated by 21° (as can be seen from the complementary angle between the line connecting (0000) with $(0\bar{1}11)_{CdS}$ and connecting (0000) with $(\bar{1}1\bar{2})_{CIGS}$ in the FFT pattern. This rotation accounts for most of the difference in lattice parameter (seven of the 12% mismatch) across the boundary. The remainder is accommodated by the surface steps, for which there is typically an extra plane of atoms in the CdS relative to the CIGS. Finally, there is evidence of

disorder and dislocations present in the CdS. These dislocations are not clearly resolvable in the image although the lattice fringes suggest numerous screw-type and occasional edge type dislocations in the CdS layer. These defects in the CdS apparently reconcile the remaining misfit.

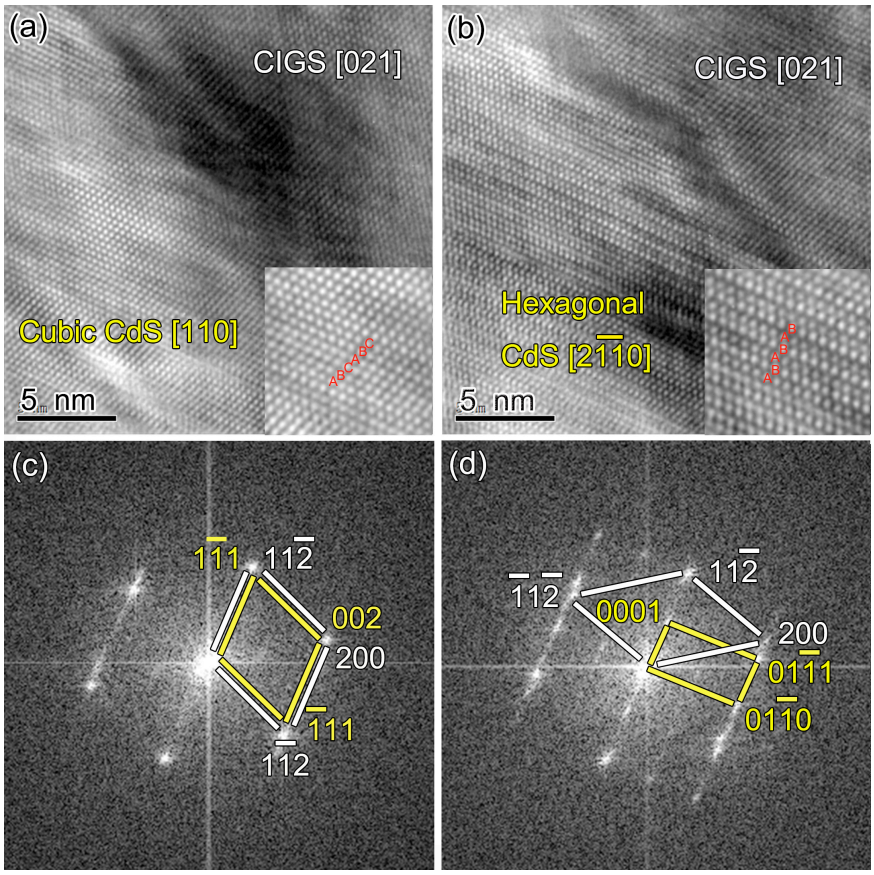

Figure 13. High resolution TEM image along CIGS [021] illustrating the hetero-interface: (a) cubic phase CdS and CIGS; (b) hexagonal phase CdS and CIGS. (c) and (d) are the FFT spectrum from (a) and (b) respectively.

Forming this relatively coherent phase boundary between the tetragonal and hexagonal phases probably involves the release of lattice strain associated with lattice mismatch and rotation. M. G. Hall *et al.*[50] showed that atomic steps could serve as major means of strain relief for Cr-rich bcc precipitates embedded in a fcc matrix of Cu-Cr alloy and are responsible for the nearly coherent grain boundaries. Thus, it is reasonable that here the atomic terraces with a regular length and height would also contribute significantly to strain accommodation between hexagonal CdS and tetragonal CIGS, leading to coherent hetero-interface and epitaxial growth of CdS on CIGS surface. Indeed this strain relief may govern, to some extent, the step spacing.

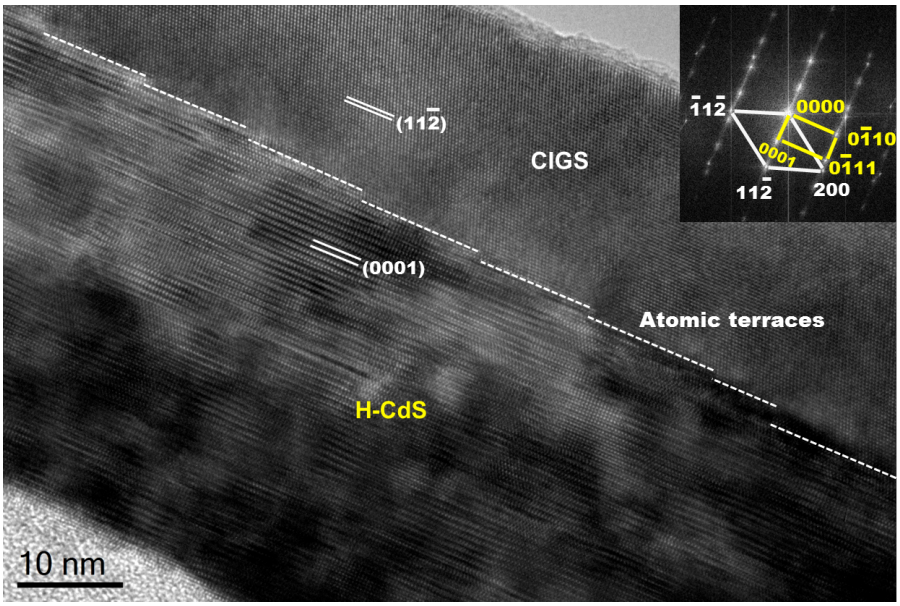

Figure 14. High resolution TEM image along CIGS [021] showing large well-defined hexagonal CdS domains epitaxially grown on CIGS. Note the atomic terraces sitting along the interface, as indicated by dashed white lines. Inset is the FFT pattern covering both CdS and CIGS, showing the epitaxial relationship between them.

Another interesting feature is that twin boundaries in CIGS can directly thread into and propagate through the whole CdS layer, as shown in Figure 15. The bottom right selected area electron diffraction pattern from the CIGS clearly shows the twin characteristics. There are hexagonal CdS domains as well as cubic phase domains, which highlights the underlying competition as to which phase would prevail. Due to the similarity of lattice constant between cubic CdS ($a = b = c = 0.583$ *nm*) and the CIGS studied here ($a = b = 0.572$ *nm*, $c/2 = 0.570$ *nm*), twins propagating from the CIGS into the CdS are more energetically favorable in the cubic phase than the hexagonal phase. In this case CIGS twins act as a template for cubic twin growth and may be responsible for stabilizing the cubic CdS locally around the twin (as in Figure 15). During the initial stage of CdS growth, a high density of stacking faults (SF) are generated probably to relieve residual misfit and accommodate the CdS cubic phase growth at the heterojunction, as seen in cubic CdS domains labeled “CdS I”. One can note the diffuse twin boundary in the CdS resulting when the two CdS I domains coalesced. The relatively irregular nature of the twin boundary in this region suggests that it only formed when the disparate CdS I grains came together. After the CdS I domains coalesced and growth could occur across the twinned region, a much better cubic domain formed including a very well-formed twin, labeled CdS II. The CdS II domain has a much lower density of stacking faults and grew epitaxially on CdS I domains. From the top right inset, the {111}-type twin boundary is clearly shown although there are some stacking faults along the other set of {111} planes. The behavior described here for the image in Figure 15 is more complex than that shown in Figure 12. In that image the grain boundary is indistinct and inclined with respect to the image zone axis. However, in that

case both the cubic and hexagonal CdS lattices appear very close in lattice spacing to the CIGS with a very small tilt angle between the two structures.

The twin boundary penetration from CIGS into CdS could be regarded as a direct consequence of CdS epitaxial growth on CIGS. This suggests that the surface structure of CIGS plays a critical role in determining the crystallinity of the CdS buffer layer. There have been many discussions concerning the beneficial role of grain boundaries in poly-crystalline CIGS compared to its single crystal counterpart. Several models and experimental evidence[51,52,53,54,55] have been provided to justify the importance of grain boundaries in reducing the recombination rate of photo-generated carriers. It is possible the grain boundaries (including twin-boundaries) in CdS may also have a significant effect on the carrier separation behavior. For example, no photocurrent is normally observed from CdS in devices. Collecting this current represents an opportunity for significant enhancement in photocurrent and device performance in both CIGS and CdTe devices. More focus should be directed to address this issue since little is known about the effect of grain boundaries in epitaxial CdS films on CIGS solar cell performance.

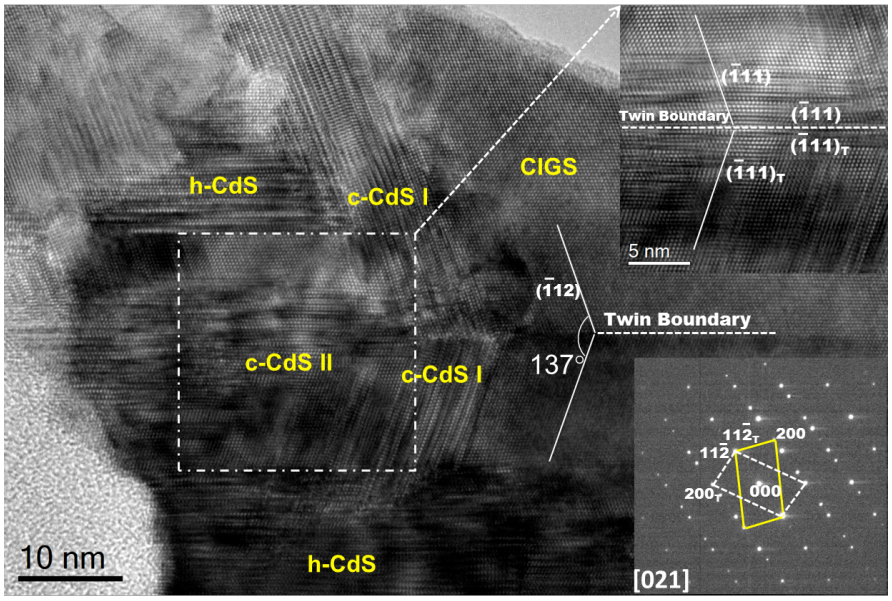

Figure 15. High resolution TEM illustrating twin boundary in CIGS propagating into CdS. Bottom right inset shows electron diffraction patterns from twins in CIGS. Top right inset is the filtered image of the region defined by dashed white lines, showing the twin relationship in cubic CdS.

Microchemistry of the Heterojunction

Cu diffusion across the heterojunction

Figure 16(a) displays a representative HREM image of the zb CdS phase on the CIGS surface. It can be seen that the interface is coherent and no notable defects were observed in the CdS other than stacking faults along (111) planes. The epitaxial

relationship is $\{111\}_{CdS}$ || $\{112\}_{CIGS}$, $(001)_{CdS}$ || $(200)_{CIGS}$, and $[110]_{CdS}$ || $[021]_{CIGS}$, as described above. STEM-EDS maps acquired in this region are shown in Figure 16(b). The most apparent feature is the uniform Cu-rich layer on the CIGS surface over the observed region. Combining with Figure 16(a), we find that the Cu enrichment roughly occurs in the region where stacking faults are found, suggesting that incorporation of Cu may build up some minor strain due to its substitution for Cd. Despite the stacking faults, however, the epitaxy is still conserved. Careful inspection of Figure 16(c) and (d) suggests that there is a Cu deficient layer in the CIGS, indicated by the oval. In this region the concentrations of Cd and Se are enhanced [see Figure 16(d)], consistent with a buried *p*-*n* homojunction as in the case of CBD-CdS/CIGS.[56,57]

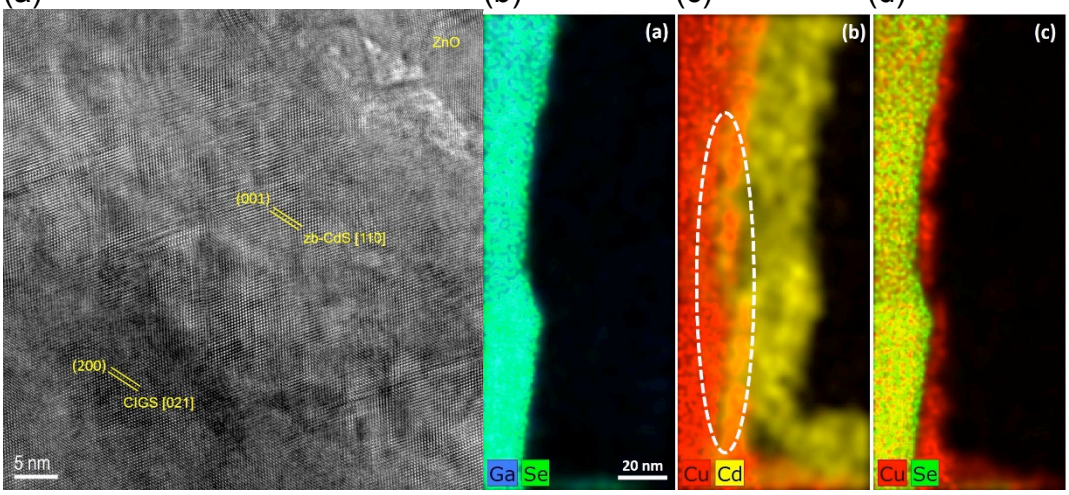

Figure 16. (a) High resolution TEM image showing zb CdS on CIGS with the epitaxial relationship indicated. (b-d) STEM-EDS maps obtained from the region shown in (a). Note the uniform Cu rich layer in CdS. The dotted white oval suggests the Cu deficient layer.

Another typical STEM-EDS map from these regions is shown in Figure 17. Interestingly, we find some local domains in the CdS where Cd is completely depleted and replaced by Cu, as indicated by the circled region in Figure 17(a). Quantitative EDS analysis reveals its composition: Cu 65.8%, Cd 0.6%, S 33.6%, which is very close to Cu_2S. Figure 18 shows a HREM image of the highly Cd-depleted region. The yellow square box corresponds to the circled region in the Cd map in Figure 17(a). From the fast Fourier transform (FFT) of the image in the boxed region (see inset) the structure can be determined and is described well by cubic Cu_2S with lattice parameter a = 0.561 nm, consistent with the Cu_2S powder diffraction file card number 00-053-0522. Thus, in some cases the heterojunction partner material in some portions of the heterojunction is apparently Cu_2S, epitaxially grown on the CIGS with the same orientation relationship as discussed above for CIGS/zb-CdS. Cu_2S is a known *p*-type semiconductor with a band gap of about 1.15 eV and was widely studied for CdS-Cu_2S solar cells.[45,58] It has a comparable band gap to CIGS and can potentially form its own collecting heterojunction with the CdS surrounding it. As with CdS, Cu_2S contains a large number of defects and thus is not expected to yield significant photocurrent, as observed.

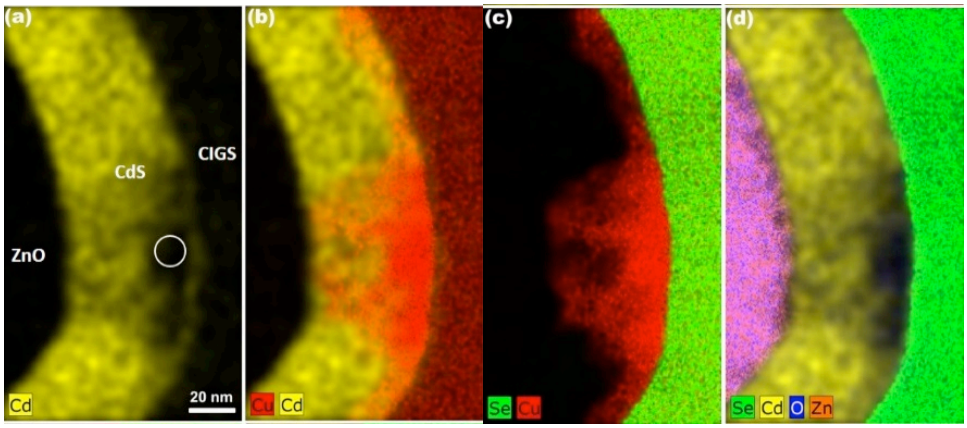

Figure 17. STEM-EDS maps showing completely depleted Cd region (indicated by the circle in (a) filled by high concentration Cu.

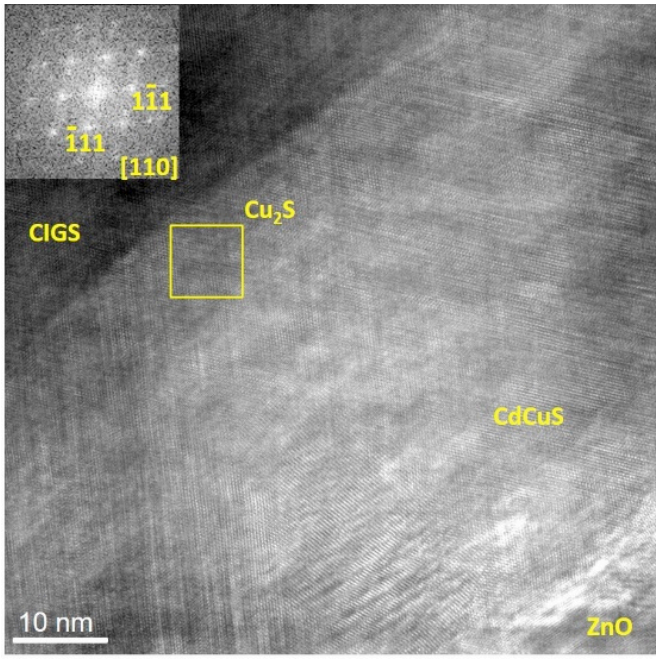

Figure 18. HREM image of highly Cd depleted region. The region indicated by the yellow square box, which can be well indexed according to cubic Cu_2S from FFT inset, corresponds to the circled region in Figure 17(a).

Composition depth profiles across the heterojunctions were constructed from the EDS analyses such as shown in Figure 16 and Figure 17 and are displayed in Figure 19. The profiles show clear evidence of Cu penetration into the CdS. The results are similar for both zincblende and wurtzite CdS. Which of these two phases form is determined by the surface orientation of the CIGS on which the CdS grows (see discussion above).

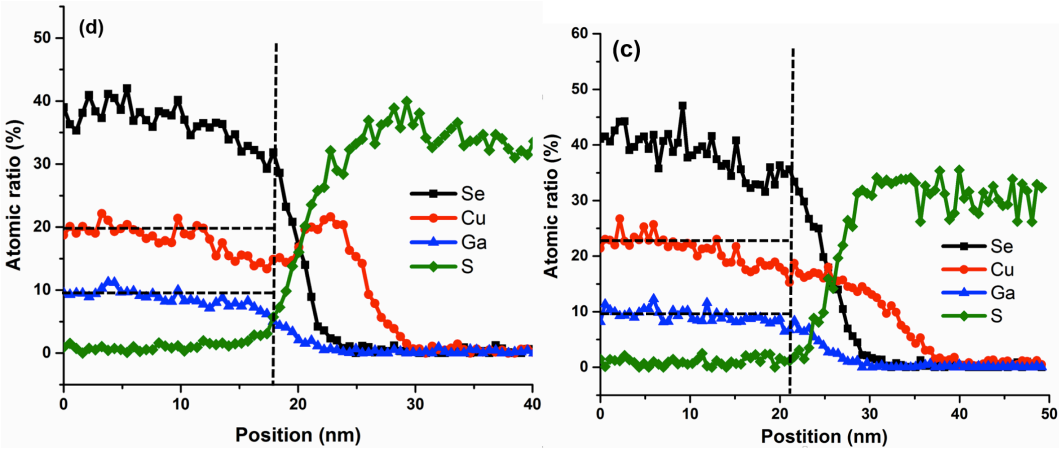

Figure 19. Composition profiles for (left) zincblende and (right) wurtzite CdS constructed from EDS maps such as shown in Figure 16.

The composition profiles measured by STEM-EDS were further validated by SIMS analysis of the materials. SIMS measures atomic concentrations averaged over large areas on the order of microns squared or larger, so it is less susceptible to finding phenomena that only occur in a very localized region. However, SIMS cannot detect atomic-scale variations in compositions and also is susceptible to artifacts arising from the sputtering of the material, particularly since these samples have rough interfaces from the polycrystallinity. The sensitivity limits of SIMS and STEM-EDS are different as well; most notably for our purposes, SIMS can measure H content in the films, while EDS cannot detect H.

Analysis of the films described above showed strong Cu signal in the majority of the CdS layer. Ascribing a quantitative difference in depth of penetration of the different elements measured by SIMS depends somewhat on how the signals are made comparable (for example by normalization of signal levels). An example profile is given in Figure 20. Here the ZnO profile is calculated from the average of the Zn and O signals. The CdS profile is an average of the Cd and S signals and the CIGS profile is based on the average of In, Ga, and Se. The signals were further normalized such that the sum of the ZnO, CdS, and CIGS values totaled one. The bare Cu signal is normalized to 0.33 to represent its nominal fraction in the CIGS and overlayed to allow comparison of its depth profile to those of the major materials in the stack. In the STEM-EDS measurements the Ga and Se profiles are very abrupt at the CIGS/CdS interface. This is similar to the SIMS result that shows a very abrupt rise in the Se signal, although the Ga signal increases more slowly, suggesting a Ga-depleted region near the interface. The

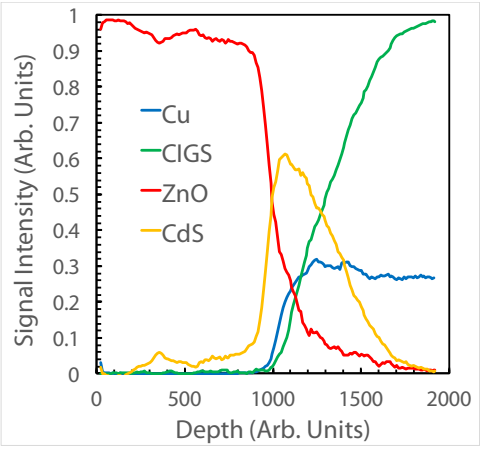

Figure 20. The average of two SIMS depth profiles (for sample G21) showing the distribution of materials in the device.

striking feature is that the Cu signal rises nearly 200 seconds earlier in the sputter depth profile, corresponding to ~70% of the thickness of the CdS layer or ~30 nm of penetration of the majority of the Cu into the CdS. This is consistent with the STEM-EDS and confirms that the observation of Cu in the CdS is not a local phenomenon, but rather occurs over broad areas. Since the SIMS measurements are averaged over large areas and also involve complex interactions among the sputter beam and the atoms of the sample, quantitative analysis by SIMS is less reliable than the STEM-EDS measurements, but rather provides qualitative confirmation that the composition profiles obtained with STEM-EDS from only a few positions on the sample represent the composition profile across more macroscopic dimensions. The calibrated STEM-EDS composition measurements are considered quantitative, at least to a level below the noise in the line profiles, shown for example in Figure 19 (<1%), and also are resolved to near-atomic level.

Measuring the bandgap of buffer layers in CIGS solar cells at high resolution is crucial for understanding device performance. The traditional approach is to measure the optical absorption. This offers high energy resolution but suffers from low spatial resolution and is difficult to apply for thin layers (tens of nm). We were able to directly measure the energy gap of the Cu_2S domains in the buffer layer from valence band electron energy loss spectroscopy (VEELS) data obtained from those domains. The energy resolution of the VEELS instrument was determined to be ~100 meV based on the full width at half maximum (FWHM) of the zero loss peak. The lateral resolution in the current measurements was limited by inelastically scattered electrons in the low energy loss regime and was estimated to be ~1 nm for the measurements here. A VEELS line scan was conducted across the CdS, Cu_2S layer and into the ZnO to identify the boundaries of the Cu_2S layer in the VEELS spectrum. We found the VEELS spectrum acquired from the middle of the Cu_2S domain shows no features of the VEELS low loss parts either the CIGS or ZnO, suggesting that the VEELS data is suitable for extracting the bandgap of the Cu_2S. A typical VEELS spectrum with the detailed low loss part is shown in Figure 21. Here we follow the method proposed by Park *et al.*[59] where they used linear fit to retrieve the bandgap values. Using this method we determined the bandgapvalues for the ZnO in this device to be ~3.3 eV, which is equal to the reported value 3.3 eV, indicating the validity of the method. The bandgap of Cu_2S was determined to be around 2 eV using this method, as indicated in Figure 21. The CdS exhibited a bandgap of 2.3 eV, which is also consistent with expected values after accounting for the modest amount of oxygen and other elements in the CdS material.

Elemental intermixing was studied further in the sample deposited under high oxygen level in the working gas (G19 in **Table II**) using energy filtered imaging in the STEM. In this measurement a specific energy loss region, associated with interaction with a specific atomic species. A STEM image of Sample G19 is shown in Figure 22 indicating the region analyzed by energy filtered imaging. Typical energy filtered images for this sample are shown in Figure 23.

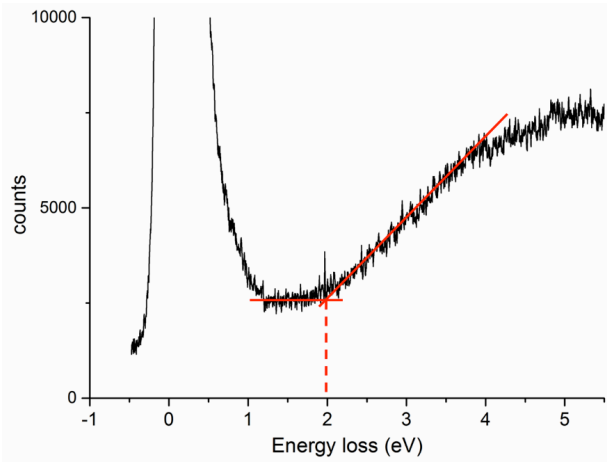

Figure 21. VEELS spectrum obtained from the Cu_2S showing a bandgap ~ 2 eV. The VEELS spectrum was obtained where no apparent interference from CIGS and ZnO

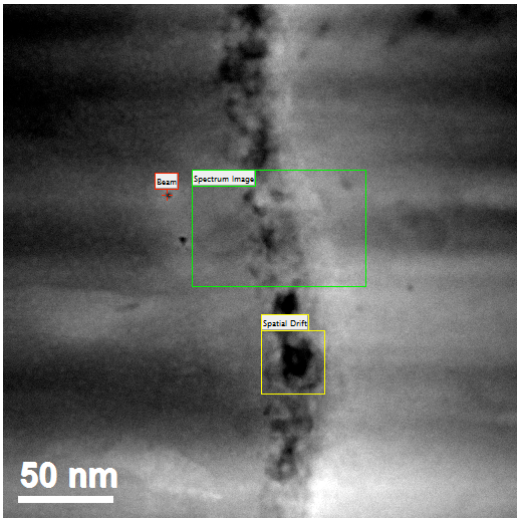

Figure 22. A STEM image obtained in angular dark field imaging mode. Energy filtered images were measured in the region indicated by the green box.

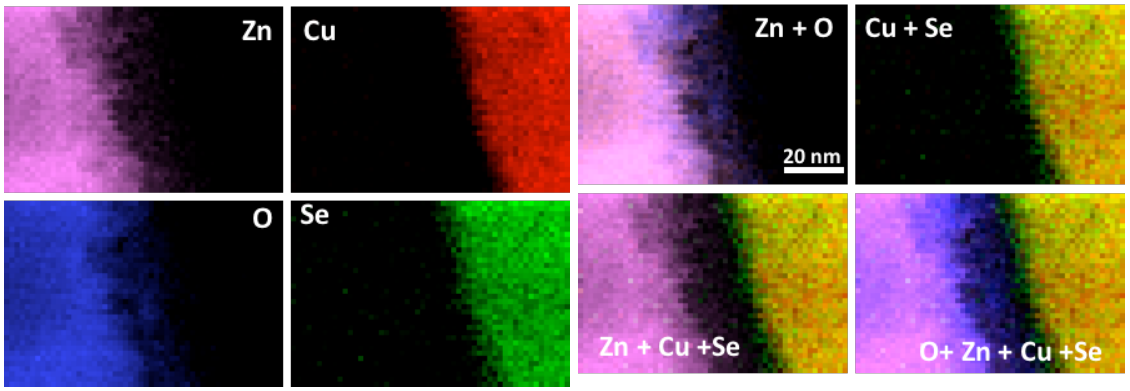

Figure 23. Energy filtered images from the green box in Figure 22 for individual elements (left four images) and showing overlap of the individual elements to emphasize that there is little Cu transfer into the CdS layer but substantial O encroachment into the CdS. The results are consistent with the EDS analysis.

We also obtained EDS maps on CBD-CdS/CIGS heterojunctions, the only difference of which with the PVD-CdS/CIGS is the deposition of CdS. Figure 24 shows the result where Cu is seen to extend beyond the Se. This observation is consistent with the results reported by Nadenau *et al.*[60] and suggests some similar chemical transfer processes between CBD and PVD deposition of CdS that can promote Cu migration from CIGS into CdS occurred. In general the Cu in the CBD material is less well organized into a clear layer with strong Cu signal. Rather, the Cu is distributed into the CBD-CdS but in a more patchy distribution, consistent with the nanocrystalline nature of the CBD-CdS which would favor less anisotropic transfer of Cu.

Cd diffusion across the heterojunction

In addition to diffusion of Cu, Cd was found to mix across junctions in ways that depend on process conditions. In the PVD-CdS/CIGS heterojunctions we studied in which a relatively low amount of O_2 was added to the process gas, Cu rich domains were consistently observed as described above. At the same time, a Cd-containing region was found to extend beyond the S signal into the CIGS surface. Our results differ from the observations by Abou-Ras *et al*.[53] where no Cd was found on the CIGS side of the heterojunction. Although only low amounts of O_2 were used in the process gas during deposition of the CdS, there is an O-containing region, roughly equivalent to the Cd-containing region, in the CIGS. The O doping probably results from diffusion into the CIGS surface when the CIGS film was exposed to sputtering gas containing mixture of O_2 and Ar. The presence of O in the CIGS surface was also confirmed by Auger electron spectroscopy.

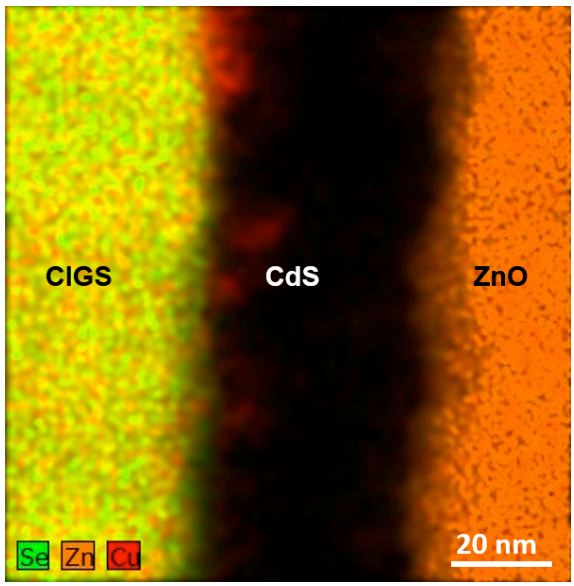

Figure 24. A typical STEM-EDS map of a CBD-CdS/CIGS heterojunction where Cu rich domains are found in CdS.

With the gradual increase of Cd concentration on the CIGS side, the Cu and Ga concentrations decrease, with Cu decreasing much more than the Ga. This is very similar to the report by Cojocaru-Miredin et al.[61] for CBD CdS where, using atom probe tomography, they found a Cu and Ga depleted region about 1 nm thick in the CIGS and doped by Cd. However, they found no Cu rich domains in the CdS. The doping depth of Cd in the CIGS that we find is at least 15 nm. Our results suggest that Cd ions may reside on Cu sites, Cd_{Cu}^{+}, which act as donors to convert the *p*-type CIGS to *n*-type. In addition, our EDS line profiles suggest the substitution of Cd for some of the Ga, Cd_{Ga}^{-}, which is an acceptor. Considering the fact that the Cu concentration is about twice as high as Ga, and Cu is more depleted, the overall doping effect still gives an *n*-type CIGS surface. These results were roughly the same for the zincblende and wurtzite CdS.

Addition of larger amounts of O_2 to the process gas significantly suppresses the formation of Cu_2Se domains in the CdS and at the highest levels it apparently effectively eliminates Cu diffusion from the CIGS into the CdS. Under these conditions, Cd can also be present in the CIGS surface layer, although with much shorter doping length than when large amounts of Cu outdiffusion occured. Figure 25(a) displays a STEM-HAADF image of zb-CdS/CIGS heterojunction where a bright band in the CIGS surface is clearly seen as indicated by two arrows, implying that the bright band should have higher average atomic number, *Z*, than the CIGS below, since image intensity in the HAADF image follows a dependence of $Z^{1.7}$ [62].

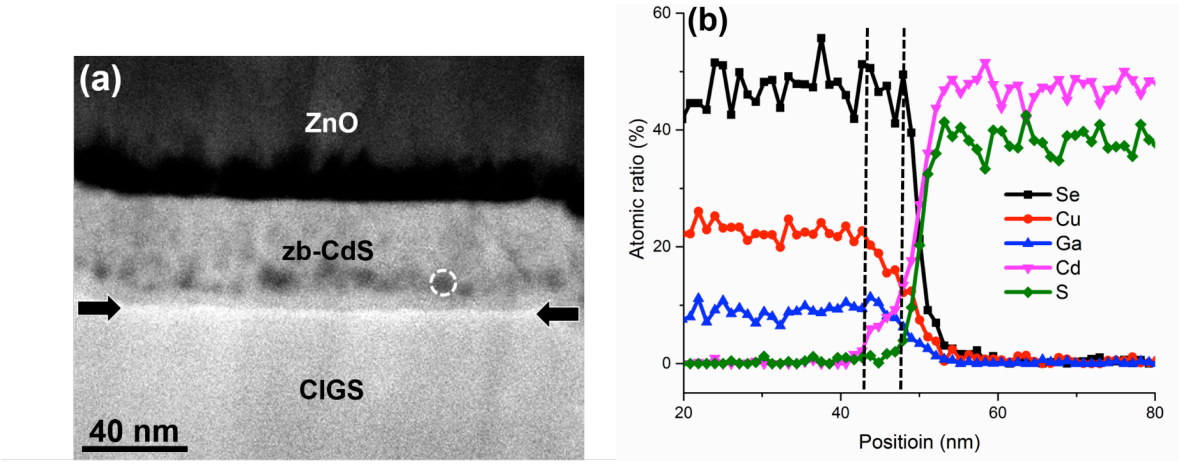

Figure 25. Low magnification STEM-HAADF image (a) of a zb-CdS/CIGS heterojunction with no Cu domains in the CdS. (b) Composition line profiles from the zb-CdS/CIGS heterojunction indicate Cd doping to ~5 nm depth in the CIGS.

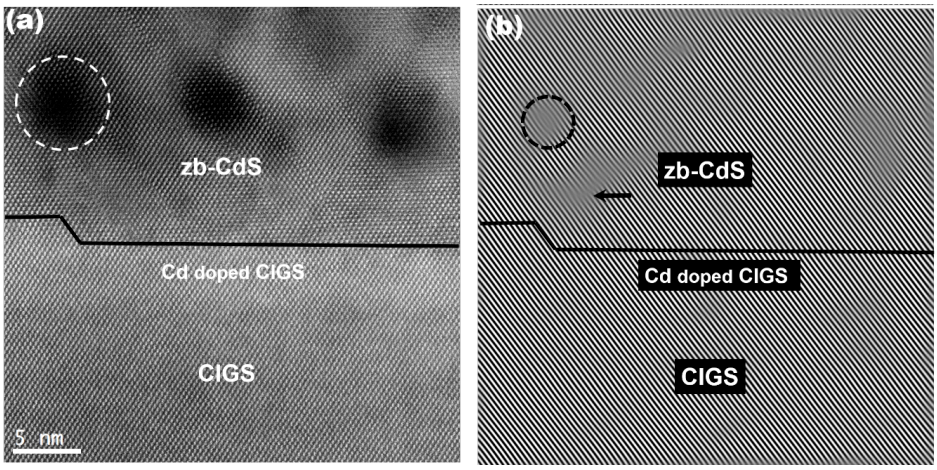

Figure 26. Atomic resolution HAADF image (a) of the zb-CdS/CIGS heterojunction shown in Figure 25(a). (b) Filtered lattice fringes using one pair of {111} reflections of CdS and {112} reflections of CIGS.

To find out the underlying chemical difference responsible for the bright band, a composition EDS line profile was measured [Figure 25(b)]. The two dotted lines mark the pure CIGS surface where the Se concentration is constant and Cd is observable above background. It is also worth noting that the Cu and Ga concentrations decrease while the Cd concentration is increasing, suggesting Cd resides on both Cu sites and Ga sites, as in the low-oxygen case discussed above. The Cd doping length for the high oxygen sample is about 5 nm, larger than the 1 nm reported in Ref. [61] but lower than for the low oxygen samples.

Our results suggest that chemical migration behaviors similar to those in CBD-CdS/CIGS occurred in the PVD-CdS/CIGS heterojunction. The fact that the Cd doping in the CIGS surface occurs even with no Cu rich domains in the CdS phase suggest that Cu vacancies are formed prior to the deposition of the CdS. A Cu depleted CIGS

surface could be formed due to the reconstruction of the CIGS surface to reduce the electric dipole energy, as supported by density functional theory calculations by S. B. Zhang *et al*.[63]

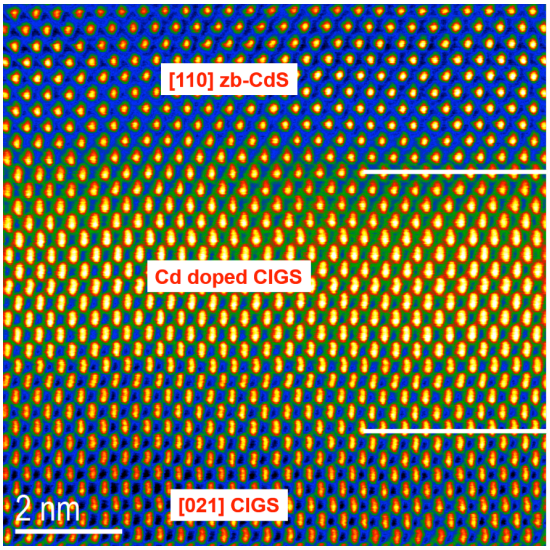

Figure 27. Colored HAADF image showing detail of the zb-CdS/CIGS heterojunction in Figure 26.

Figure 26(a) depicts atomic resolution HAADF images along [021], a zone axis of the CdS/CIGS heterojunction containing the bright band in Figure 25(a). The Cd doped CIGS surface region of about 5 nm thickness is identified based on the intensity variation and the EDS compositional line profile in Figure 25(b). The interface between the CdS and the Cd doped CIGS is sharp and free of any dislocations. Filtered lattice fringes using a pair of (-111) CdS diffraction spots (these overlap with (112)-type reflections from the CIGS) are shown in Figure 26(b) where the line indicates the interface. No misfit dislocations are found along the interface. In addition, the fringes are very coherent across the CdS and CIGS interface and of almost equal interplanar distance, suggesting good lattice match of the CdS and CIGS. The incorporation of O into the CdS enables large flexibility in tuning the lattice constant of the CdS and helps to form a coherent and defect-free hetero-interface with the CIGS. Further, we note that there are an array of dark domains about 7 nm away from the hetero-interface as shown by circles in Figure 26(a). EDS quantification suggests a composition in the marked area of: 29.1% O, 30.9% S, 40% Cd. These highly oxidized CdS domains are well crystallized and show coherent lattice fringes with the surrounding CdS matrix. As indicated by the circles in Figure 26(b), a Frank dislocation loop is formed inside the dark domain circled in Figure 26(a). The formation of the dislocation loop may be related to the agglomeration of O atoms along the {111} type close-packed Cd(O,S) planes. Another individual dislocation is also found in the CdS as shown by an arrow.

Figure 27 presents an enlarged HAADF image of the area shown in Figure 26(a) to give more insight into the CdS doped CIGS layer. The image was colored using Digitalmicrograph™ to highlight each layer according to the intensity variation. In the CdS layer, columns of Cd atoms produce the majority of the intensity with tiny tails on one side representing the O and S atoms. The dumb-bell structure of the atom columns in the CdS is clearly observed in a corresponding STEM-annular bright field (ABF) image (not shown). This mode is more sensitive for light atoms[64,65] and shows the reverse contrast to the image in Figure 27. The Cd doped CIGS layer, roughly marked by two lines, is about 5.5 nm thick, consistent with the EDS line profile shown above. The substitution of Cd for Cu and Ga as indicated by the EDS composition profile gives higher intensity in the HADDF image than the undoped CIGS below.

The Cd doped CIGS surface is also confirmed in wz-CdS/CIGS heterojunctions with no Cu domains in the CdS. Figure 28(a) displays a typical atomic resolution HAADF image

where the CdS shows complete epitaxy on {112} CIGS surface with the same epitaxial relationship as described above for wz-CdS on the CIGS. The height of the CIGS {112} surfaces from left to right across the image is about 2.4 nm which is about seven CIGS interplanar {112} spacings. The atomic steps contribute to the strain relaxation between wz-CdS phase and tetragonal CIGS. By applying image filtering using $(0002)_{CdS}$ and $\{112\}_{CIGS}$ contributions to the FFT patterns and which overlap, we identified six dislocations inside the wz-CdS as indicated by circles in Figure 28(a).

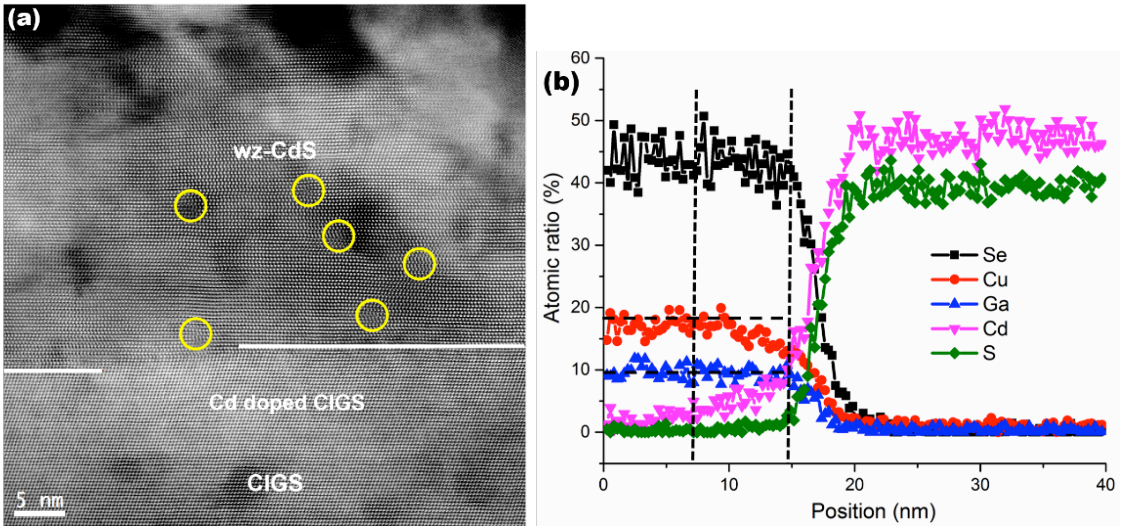

Figure 28. Atomic resolution HAADF image (a) of a wz-CdS/CIGS heterojunction. Six dislocations in the CdS are circled. (b) Corresponding compositional line profiles.

Figure 28(b) is a composition line profile extracted from the wz-CdS/CIGS heterojunction shown in Figure 28(a). The two dotted lines denote the Cd-doped CIGS region. Here, the concentration of Se and Ga are constant but Cu is reduced. This is indicative of Cu vacancy sites filled by Cd atoms. The average Cd doping length is at least 8 nm, determined from the EDS profile and the HAADF image [Figure 28(a)] where Cd doped CIGS shows slightly higher image intensity. The doping length (8 nm) here is also smaller than that in the CIGS surface in the wz-CdS/CIGS heterojunction with Cu rich domains (18 nm), supporting our observation that Cu migration from the CIGS into wz-CdS facilitates Cd doping of the CIGS surface.

To put the above results in context we compare the results for the same absorber layers but with CBD CdS rather than PVD CdS. Figure 29 shows a STEM-EDS line scan across a CBD-CdS/CIGS heterojunction. We observed O in both the CIGS surface and CdS buffer layer (not shown). Cu was also found in the CBD-CdS, consistent with the previous reports.[56,60] Another striking feature is that the S signal extends far into the CIGS, which is not seen in the PVD-CdS/CIGS heterojunctions. S diffusion into the CIGS was first observed by Heske et al. where they reported by using surface-sensitive X-ray emission and photoelectron spectroscopy that S and Se ions can go through some degree of ion-exchange. In contrast to the PVD samples, Cd was found to be present in the CIGS at much lower concentration (4% vs. at least 10%, close to the CdS|CIGS interface).

The results are in contrast to the observation by Abou-Ras *et al.*[53] where they found no Cd in the CIGS surface in a PVD-CdS/CIGS heterojunction, suggesting that elemental intermixing occurring between the CdS and CIGS can be very sensitive to the details of the growth conditions and should be discussed on a case by case basis. Recently it was shown[66] that the CBD-CdS/CIGS solar cells fabricated on flexible polyimide substrates can deliver 20.4% efficiency. The authors argued that the key of the success is that KF post deposition treatment of the CIGS surface before deposition of CBD-CdS results in a Cu and Ga depleted CIGS surface region where a p-n homojunction is generated by Cd incorporating into Cu vacancy sites and thus forming Cd_{Cu} donors. Apparently Our PVD-CdS process is producing a CdS/CIGS hetero-interface similar to the KF post deposition treatment of the CBD-CdS/CIGS solar cells.[66]

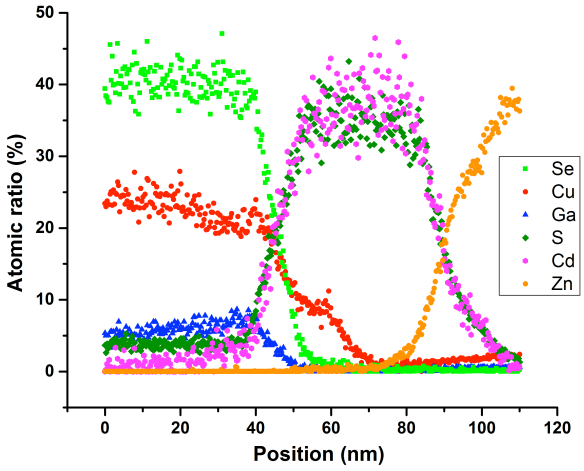

Figure 29. STEM-EDS line profiles of a CBD-CdS/CIGS heterojunction. Cd is found in the CIGS surface layer at much lower concentration than in the PVD-CdS/CIGS junctions. Note that unlike in the PVD samples the S signal is present at ~5 at.% deep into the CIGS.

Computational Results for T-6

T-6: Calculate effects of Zn alloying

We expanded this task to include the full quaternary CdZnOS space to treat the influence of O. This was to provide an extra degree of freedom to identify alloys that may beneficially shift the valence band edge to lead to the desired properties of a favorable conduction band offset and a larger band gap that pure CdS. Our initial investigations into CdS and ZnS identified that without O, Zn alloying would likely lead to a much larger conduction band spike than is tolerable in high-performance CIGS photovoltaics.

Thermodynamic, Optical, and Electronic Properties of CdZnOS alloys

Our analysis of CdZnOS alloys for candidate buffer layers focused on several properties relevant for good performing solar cells. Specifically, we studied the optical band gap, the conduction band offset with the absorber and window layers, the dopability of the buffer, the interface quality as defined by the lattice match with the absorber, and the thermodynamic stability of the buffer as a function of composition. These parameters alloy us to assess which compositions may best satisfy the number of constraints that are critical to achieving higher efficiencies in real photovoltaic devices. For example, at the simplest level, alloying can influence the lattice constants of the buffer that lead to higher-quality interfaces with CIGS, as shown in Figure 30. It has also been shown that the degree of doping within the buffer can play an extremely important role in overall

performance, and has a strong influence on the effects of other critical parameters such as the conduction band offset.[67] This complexity and interaction between different variables illustrates the difficulty in optimizing performance. To provide additional insight into how alloying may yield better buffers, we have expanded our model to estimate how specific compositions correlate to dopability. Our model is based on the concept of intrinsic doping-limits in semiconductors that are intimately related to their band edge positions on an absolute energy scale[68] and incorporates our calculated properties for Fermi-pinning energies into a model for the free carrier concentration. Specifically, we solve the equation

$$n(\varepsilon_F) = \frac{\sqrt{2m_e^{*3}}}{\pi^2\hbar^3}\int_{E_{CBM}}^{\infty} d\varepsilon \frac{\sqrt{\varepsilon - E_{CBM}}}{1+e^{(\varepsilon - \varepsilon_F)/kT}}, \quad (2)$$

where k is the Boltzmann constant, T is the temperature, m_e^* is the effective electron mass, ε is the electron energy and E_{CBM} is the energy of the conduction band edge. For the effective masses we linearly interpolate values for the alloys based on the composition and for calculated values of 0.21, 0.21, 0.23 and 0.25 the mass of the free electron for CdS, CdO, ZnS, and ZnO, respectively, as determine from the electronic band structure. This analysis assumes a parabolic conduction band, but an extension to accounting for non-parabolicity of the conduction band leads to only slightly larger carrier concentrations and does not influence our overall conclusions. This effect also has ramifications on the optical absorption in the buffer due to band-filling effects for certain compositions that are predicted to be highly doped. We show these modeled effects in Figure 31, which shows the calculated optical band gap as a function of composition, for the case of no band-filling [Figure 31(a)] to highly-doped material [Figure 31(c)]. Our results predict that O-rich material is expected to suffer from a blue shift due to larger resulting carrier concentrations.

In addition to calculating proxies for the interface quality and optical absorption of the buffer (see Figure 30 and Figure 31), we also explored how composition influences the band edge positions and the resulting conduction band offset (CBO) with the absorber. This parameter has been strongly linked to macroscopic device performance, and we include our calculated conduction and valence band offsets with respect to pure CdS in Figure 32. Our results confirm why ZnS exhibits such unfavorable performance due to a large conduction band spike that limits electron transport, and we identify that modest Zn content can be used to tune the CBO to optimal levels, depending on the Ga-content in the absorber. The influence of O is founds to primarily decrease the bandgap and increase the electron affinity relative to pure CdS, which implies that only a combination of O and Zn is likely to maintain a similar CBO as CdS and lead to good performance.

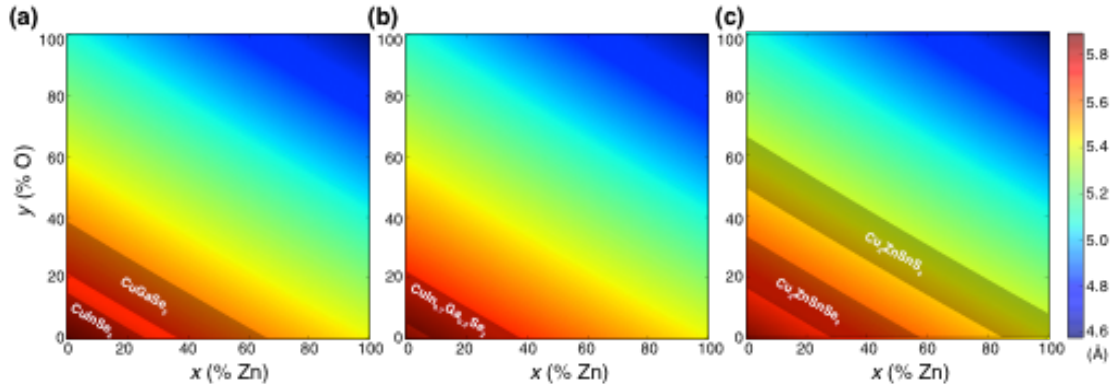

Figure 30. Lattice constant maps for zincblende $Cd_{1-x}Zn_xO_yS_{1-y}$ solid solution shown as a function of the O and Zn content over the quaternary phase space, and assuming Vegard's Law. Shaded regions are included in each panel for a reference absorber lattice constant with a tolerance of ±1% lattice mismatch with respect to the buffer using the values in **Table IV**. The shaded references represent the a lattice constants of (a) pure $CuInSe_2$ and $CuGaSe_2$, (b) the emerging absorbers Cu_2ZnSnS_4 and $Cu_2ZnSnSe_4$, and (c) their respective alloys of $CuIn_{0.7}Ga_{0.3}Se_2$ and $Cu_2SnZn(S_{0.4}Se_{0.6})_4$ that yield desirable band gaps of ~1.2 eV. The four corners in each panel represent the bulk lattice constants of CdS (lower left), CdO (upper left), ZnO (upper right), and ZnS (lower right). ZnS (lower right).

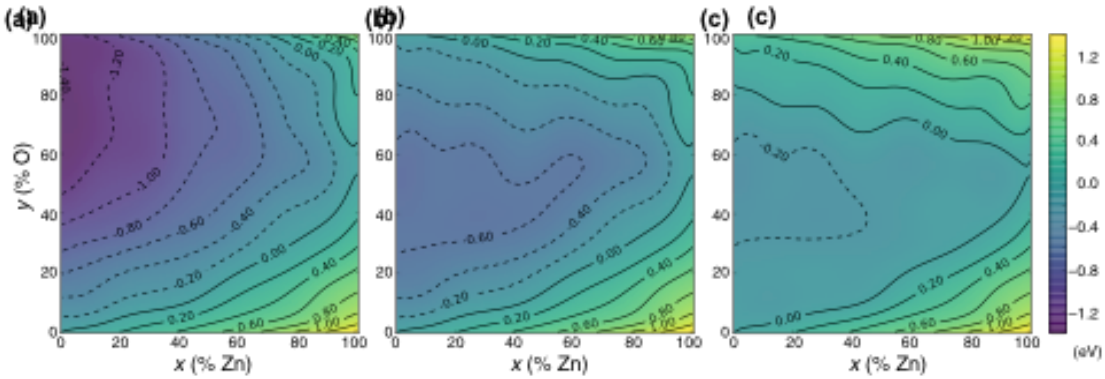

Figure 31. Maps of the calculated fundamental (a) and estimated optical (b,c) band gaps for zincblende alloys shown as a function of the O and Zn content over the quaternary phase space. Due to the high carrier concentrations predicted for certain regions of the alloy space, we expect Burstein-Moss shifts in the optical absorption onsets as seen by the differences in (b) and (c) relative to (a). The optical band gaps are obtained by combining the fundamental band gaps (a) and the predicted Fermi pinning levels with respect to the CBMs from the calculated CNLs from the branch-point energies (b) and the hydrogen-related pinning levels (c) and offer reasonable bounds to estimate possible doping-induced blue-shifts.

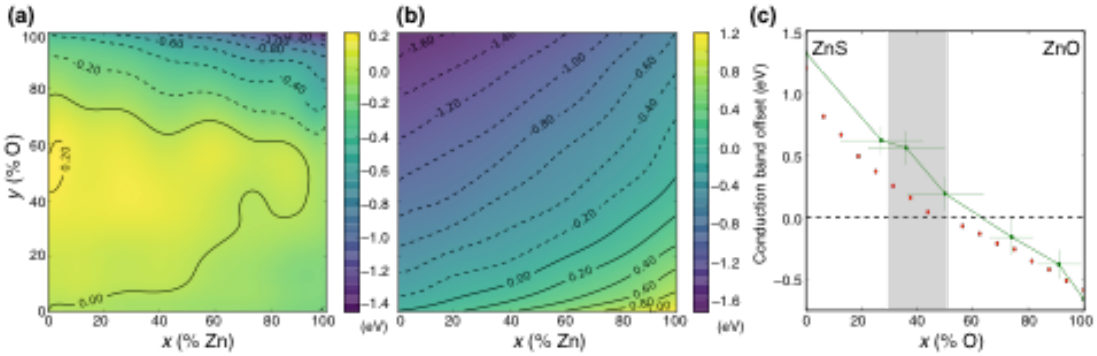

Figure 32. Maps of the calculated valence band offsets (a) and conduction band offsets (b) for zincblende alloys shown as a function of the O and Zn content relative to the pure CdS values. All values over the quaternary phase space assume the corrected band gaps from Figure 31. The CBOs of the zincblende Zn(O,S) system relative to CdS are shown in (c), with experimental values extracted from Ref. 69 (green points) for ALD-grown films on Cu_2O with errors estimated from the reported O and S content. The conduction band positions of the calculated and experimental data are both aligned to a CdS reference, assuming transitivity holds for the Cu_2O/CdS and Cu_2O/Zn(O,S) heterojunctions. The region of 50-70% S/(S+O) of Zn(O,S) is shaded to highlight the typical composition range obtained in CBD-grown material.

Physical and Electronic Structure of Competing Phases to (Cd,Zn)(O,S) Solid Solutions

Another critical aspect to this study is the stability of the alloys and the tendency to phase separate. We include the enthalpy of mixing over the quaternary space in Figure 33 for wurtzite alloys. We note that these alloys are thermodynamically stable for nearly all compositions, but rocksalt phases become more stable in the O- and Cd-rich regime as denoted by the dashed white line in Figure 33(a). The data indicate that a positive enthalpy of mixing exists over the entire quaternary space and that high growth temperatures are necessary to stabilize certain compositions, particularly for compositions that are more Zn-rich with intermediate O contents. We include the full free energy of mixing at 1000K in Figure 33(b) and 1400K in Figure 33(c), which shows relatively small regions of stability for solid solution quaternary alloys. This implies that realizing certain alloy compositions may be difficult with respect to segregating into their bulk constituents or possibly other favorable Cd,Zn,O, and S-containing compounds that may form under certain conditions. To explore this further and assess possible implications of alternative phases incorporated into buffer alloys, we calculate the electronic structure and stability of CdO_2, $CdSO_4$, ZnO_2 and $ZnSO_4$, We summarize their calculated properties in **Table IV** and Figure 34 – Figure 37.

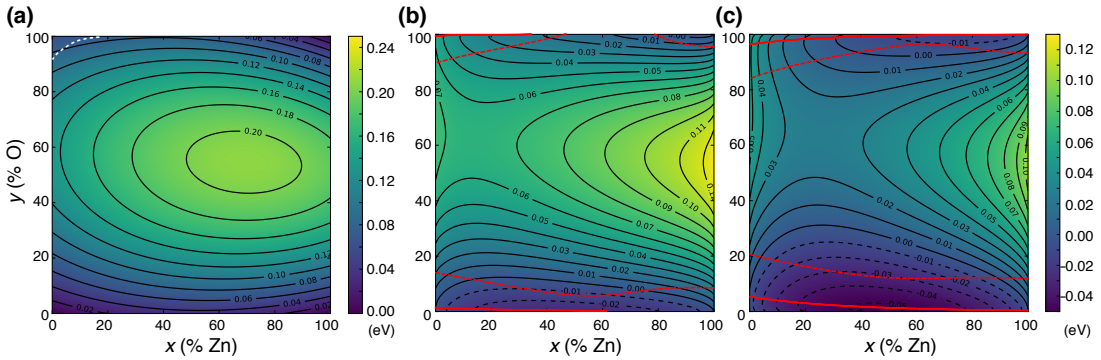

Figure 33. (a) Map of the heterostructural mixing enthalpy of the quarternary wurtzite alloys as fit within a regular solution model as described in the text. The boundary denoted by the dashed white line refers to the region where rocksalt alloys are predicted to be more favorable. The free energy of mixing at (b) 1000 K and (c) 1400 K are shown for wurtzite quaternary alloys. The solid red lines in (b) and (c) indicate the boundaries for stable compositions while the dashed dotted red lines indicate the boundaries for spinodal decomposition. The four corners in each panel represent the bulk references of CdS (lower left), CdO (upper left), ZnO (upper right), and ZnS (lower right).

We first describe CdO_2 and $CdSO_4$, which we include in Figure 34 and Figure 35, respectively. These phases are relevant for the Cd(O,S) alloys, which have been shown to lead to larger optical band gaps than pure CdS buffers in CdTe solar cells.[70] This is in contrast to our results on the Cd(O,S) solid solutions, which predict that O incorporation should lead to decreased optical band gaps. This discrepancy has been attributed to the coexistence of Cd oxide and sulfide phases within a $CdSO_4$ matrix,[71] which may be responsible for an attractive and intriguing combination of good electrical conductivity and higher optical transparency relative to pure CdS buffers. Therefore a proper characterization of the electronic structure of these phases is important to understand how the incorporation of these phases may influence charge transport in the buffer.

Both structures are characterized by Cd that are octahedrally coordinated with O, with the octahedral linked by SO_4 tetrahedra in the case of $CdSO_4$. The coordination of Cd in these materials differs from the local tetrahedral coordination of Cd in the zincblende and wurtzite phases and presents a signature that can be identified by experimental techniques such as x-ray photoelectron spectroscopy. Compared to rocksalt CdO, which also exhibits octahedrally-coordinated Cd, the local configurations in CdO_2 and $CdSO_4$ are more varied due to octahedral rotations. These types of signatures were recently identified by synchrotron-based x-ray emission spectroscopic measurements on oxygenated CdS buffers in CdTe thin film photovoltaics that suggest a variety of other stoichiometries may exist within these buffers in addition to the sulfate.[72] In addition to highlighting the importance of characterizing how these phases affect devjce performance, they suggest the existence of multiple phases is likely in the other oxysulfide buffer alloys that contain Zn.

Table IV. The calculated lattice constants, formation enthalpies, and band gaps for a number of phases spanning the Cd,Zn,O,S quaternary space. For materials that have an indirect band gap (i) the direct band gap (d) is also included.

Material	Lattice constant(s) (Å)	ΔH (eV/f.u.)	Band Gap (eV)
CdO	a = 4.73	–2.13	0.90 (i) ; 2.18 (d)
CdS	a = 4.17; c = 6.80	–1.57	2.52
CdO_2	a = 5.34	–1.66	3.07 (i) ; 3.11 (d)
$CdSO_4$	a = 8.35 ; b = 5.32 ; c = 7.25	–9.13	5.05
ZnO	a = 3.23; c = 5.24	–3.64	3.23
ZnS	a = 3.83; c = 6.09	–2.00	3.92
ZnO_2	a = 4.88	–2.51	5.46 (i) ; 5.94 (d)
$ZnSO_4$	a = 4.77 ; b = 6.75 ; c = 8.58	–9.87	7.24

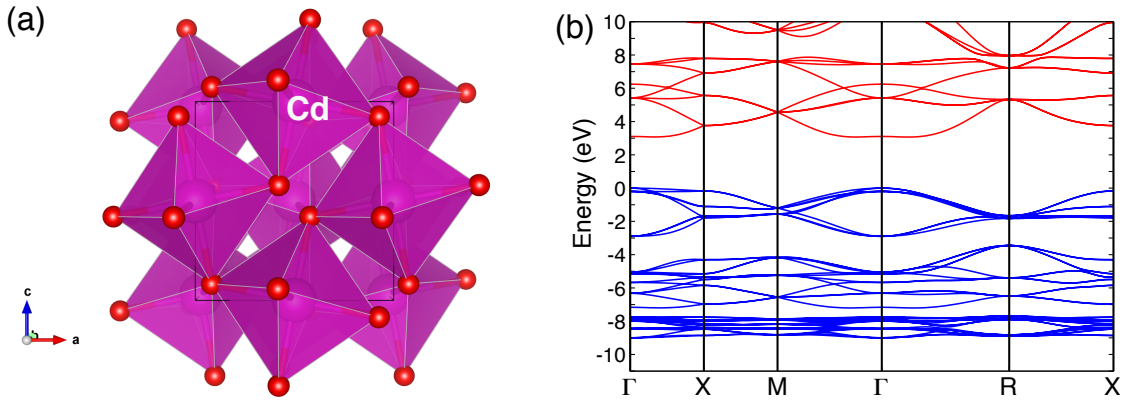

Figure 34. (a) The crystal structure of CdO_2 showing the octahedral coordination of Cd with the O atoms shown in red, and (b) its calculated electronic band structure. We find a large indirect gap that would lead to full transparency over the visible portion of the spectrum.

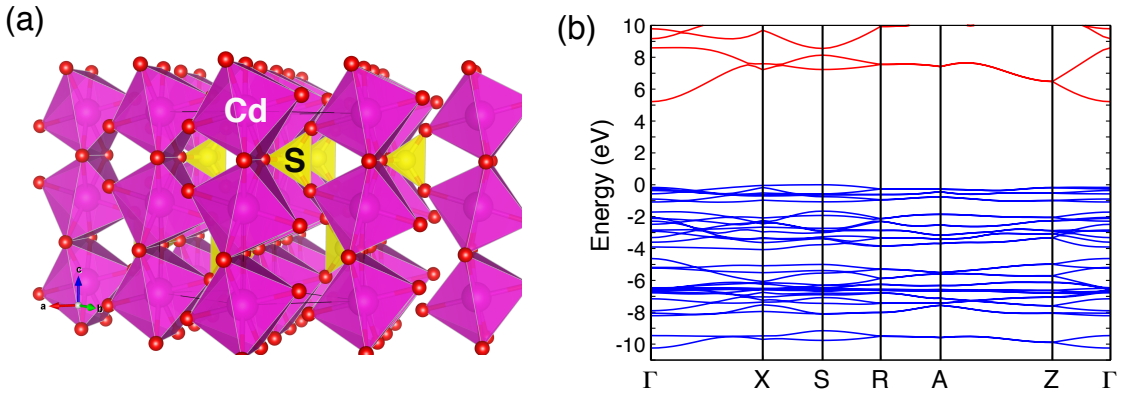

Figure 35. (a) The crystal structure of $CdSO_4$ showing the Cd-O octahedra linked by SO_4 tetrahedra, with the O atoms shown in red. (b) The calculated electronic structure reveals a large direct with an effective electron mass of ~0.45m_e.

In terms of their electronic structure, we identify both CdO_2 and $CdSO_4$ exhibit large band gaps. The calculated indirect band gap of CdO_2 is 3.07 eV and only slightly smaller than the direct gap of 3.11 eV, while the calculated band direct band gap of $CdSO_4$ is much larger at 5.05 eV. These values indicate that the formation of these phases in Cd(O,S) buffers would reduce absorption in the visible compared to CdS and CdO. In terms of their electron transport properties, we identify that the conduction band of $CdSO_4$ exhibits a pronounced dispersion despite the fact it is predicted to be an insulator. The calculated conduction band effective mass of $CdSO_4$ is found to be nearly isotropic and ~0.45m_e, which is larger than for CdO and CdS (~0.2m_e in both materials) but still quite low. This would imply that electron injection into the much-larger-gap $CdSO_4$ would still yield favorable transport properties assuming that there are not prohibitive barriers for such a process to proceed. This depends on the conduction band offsets of the $CdSO_4$ relative to the other buffer alloy constituents and will be assessed within the next budget periods. Alternative suggestions are that $CdSO_4$ acts more like a surface passivation layer and that transport through the Cd(O,S) is established through the CdS and CdO portions of the matrix,[73] which can be verified by a better knowledge of the band offsets.

Next we consider the analogous Zn-containing compounds of ZnO_2 and $ZnSO_4$, which we include in Figure 36 and Figure 37. These phases are found to be qualitatively very similar to their Cd-containing counterparts but possessing slightly larger band gaps. However, unlike in the Cd(O,S) alloys, these alternative phases are not expected to be as beneficial from the standpoint of reducing unwanted absorption over the visible portion of the spectrum owing to the larger band gaps of pure ZnO, ZnS, and Zn(O,S). As summarized in **Table IV**, the calculated band gaps of ZnO_2 are $ZnSO_4$ are 5.46 eV and 7.24 eV, respectively. Again, the ZnO2 phase is an indirect band gap material like the CdO2, while the sulfate has a direct band gap. The effective mass of the conduction band of $ZnSO_4$ is again nearly isotropic and ~0.5 m_e, which suggests good electron mobility for injected carriers, although not as mobile as in ZnO and ZnS (~0.2 m_e). Like $CdSO_4$, the extent to which $ZnSO_4$ may participate in charge transport and how it may ultimately influence device performance remains to be determined. This will be

elucidated by subsequent determination of the band edges with respect to the other buffer layer alloy constituents.

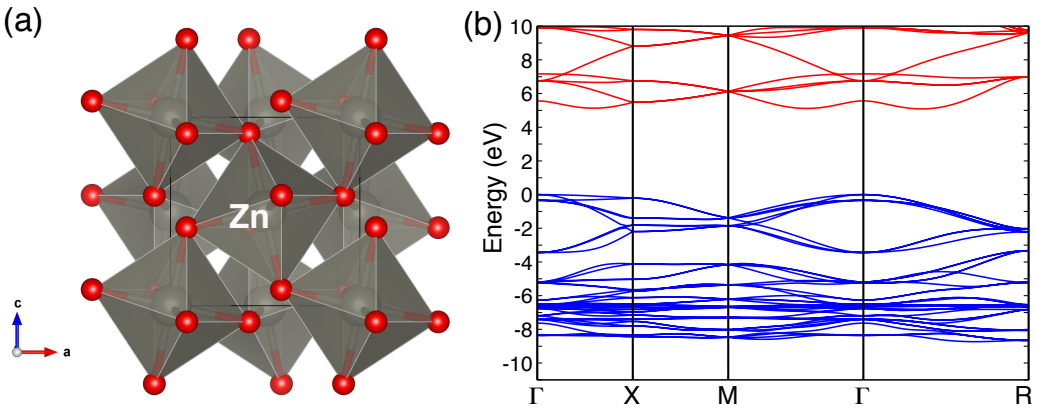

Figure 36. (a) The crystal structure of ZnO_2 showing the octahedral coordination of Zn with the O atoms shown in red. Like CdO_2 in Figure 34, the calculated electronic band structure in (b) identifies a large indirect gap.

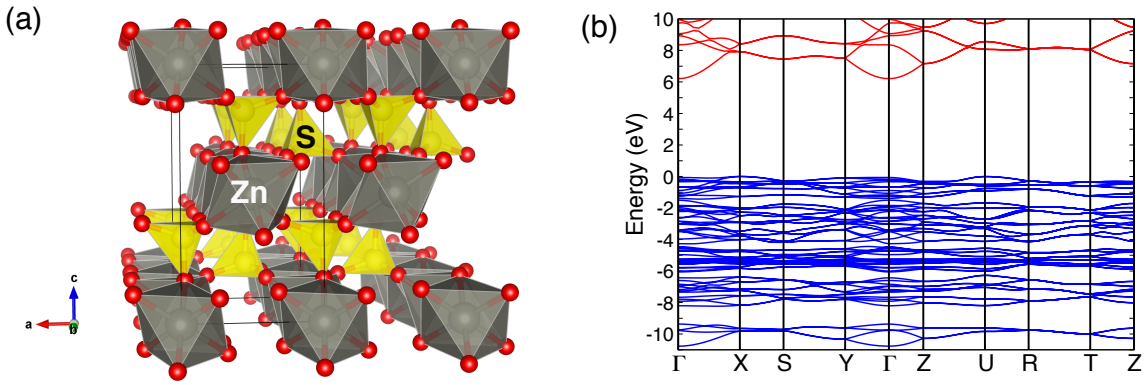

Figure 37. (a) The crystal structure of $ZnSO_4$ showing the Zn-O octahedra linked by SO_4 tetrahedra, with the O atoms shown in red. (b) The calculated electronic structure reveals a large direct with an effective electron mass of ~0.5m_e.

Physical and Electronic Structure (Cd,Mg)(O,S) Solid Solutions

In Figure 38 and Figure 39 we summarize our results for the CdMgOS alloys, identifying how the lattice constant, optical band gap, valence band offset, and conduction band offset are influenced as a function of O and Mg content. We find that the influence of Mg incorporation on the band gap and CBO is qualitatively similar to Zn, but the effects are more pronounced and result in faster increases in band gap and conduction band offsets. Specifically, there is a larger blue shift with Mg incorporation that predominantly influences the conduction band position on an absolute energy scale. We distill our results to identify optimal compositions in terms of favorable band gaps and conduction band offset with respect to CIGSe in Figure 40. We find that the qualitative features of

the optimal CdMgOS compositions follow that of the CdZnOS alloys, and that Mg fractions of ~20-30% and O fractions of ~5-15% are predicted to yield lattice-matched material to CIGSe. Our analysis of the chemical stability of the CdMgOS alloys is also included in Figure 40(b), where we find that this target composition range exhibits low mixing enthalpies and should form stable random alloys for low growth temperatures (>~400 K). Overall, our results suggest that CdMgOS alloys may be effective alternative buffer candidates to CdS and CdZnOS.

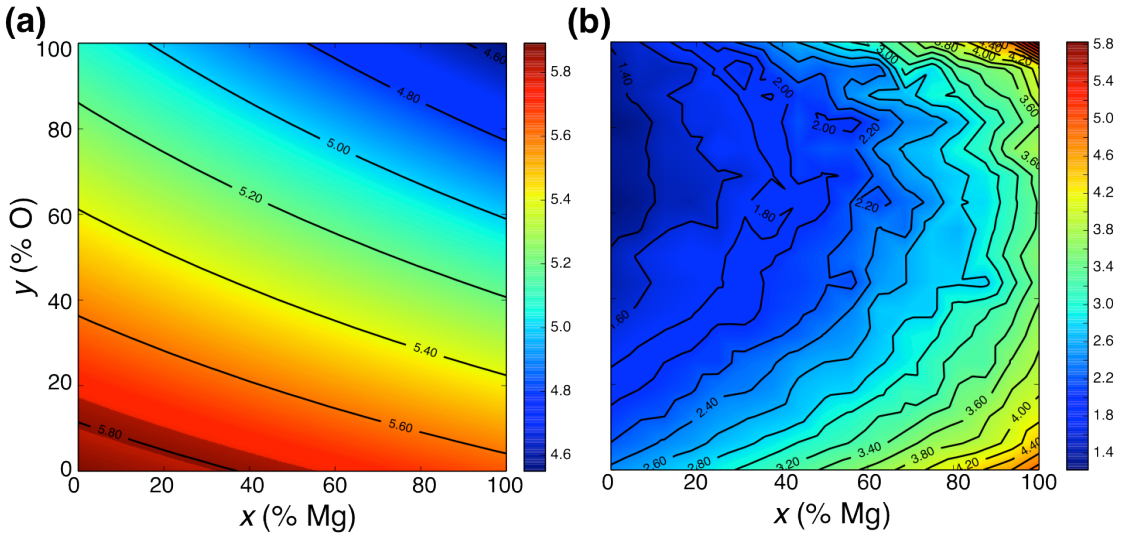

Figure 38. (a) Lattice constants for $Cd_{1-x}Mg_xO_yS_{1-y}$ alloys in the zincblende phase as determined by Vegard's Law. CdS is represented by the lower left corner. Lattice-matching with typical Ga-content Cu(In,Ga)Se_2 (CIGS) is highlighted by the shaded region. The calculated band gaps are in (b), where Mg expectedly leads to significant increases in the band gap due to the much larger band gaps of MgS and MgO.

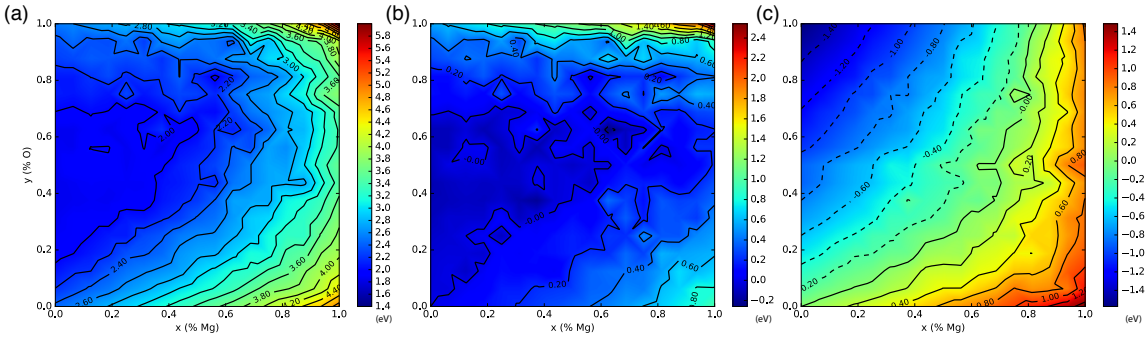

Figure 39. Maps of (a) the calculated optical band gap, (b) the brand-point energy (charge-neutrality level) with respect to the valence band edge, and (c) conduction band offset with respect to CdS as a function of composition for the CdMgOS alloys in the zincblende phase. The influence of Mg incorporation is qualitatively similar to Zn in CdZnOS alloys but the effects are stronger for a given composition.

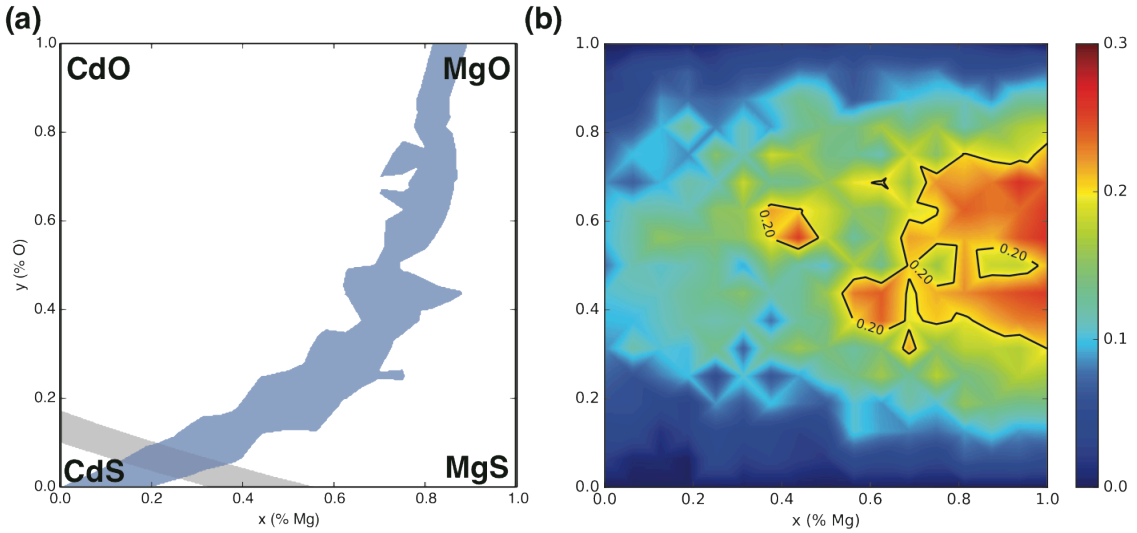

Figure 40. (a) Compositions of CdMgOS that give an optical band gap within 0.1 eV or greater than CdS and a relative CBO –0.05-0.3 eV are highlighted in blue as would be desirable for typical CIGSe alloys with band gaps ~1.2 eV. The grey band indicates the composition regions that would be lattice-matched within 1% to CIGSe. The enthalpy of mixing (ΔH) over the quaternary space is included in (b) as defined relative to the parent compounds of CdS, CdO, MgS, and MgO in the zincblende phase. The energetic cost in (b) for forming optimal CdMgOS with ~20% Mg and ~10% O from (a) is small and should be thermodynamically accessible at low growth temperatures.

Computational Results for T-7

T-7 Calculate effect of Zn and O alloying on (Cd,Zn)(O,S)/CIGS interface properties

Multiscale modeling of how alloying the buffer material influences device performance

We utilized properties calculated from our *ab initio* calculations to parameterize device level simulations using the Solar Cell Capacitance Simulation (SCAPS-1D) software and models for the MiaSolé CIGSe solar cell stack as parameterized from real devices. Our SCAPS model of current MiaSolé CIGSe devices is parameterized from both experimental and theoretical data and exhibits certain features in the quantum efficiency (QE), as shown in Figure 41. We find that several material parameters can be linked to the shoulder in the experimental QE is observed from ~400-500 nm (2.5-3.1 eV), where in Figure 41(a) we show the influence of doping and increasing the shallow donor concentration in the buffer can lead to a decrease in this lower-wavelength portion of the spectrum. In Figure 41(b) we consider other important device metrics, such as open-circuit voltage (V_{oc}), short-circuit current (J_{sc}), the fill-factor (FF) and overall efficiency, where we find that increasing the carrier concentration in typical CdS-like buffers leads to an overall improvement in performance as previously observed in other device level studies.[X1] These results overestimate the efficiency, V_{oc} and FF compared to the typically observed values in real devices [see Figure 41(b)], so there are other parameters in the device model that need to be modified to more accurately represent the real devices.

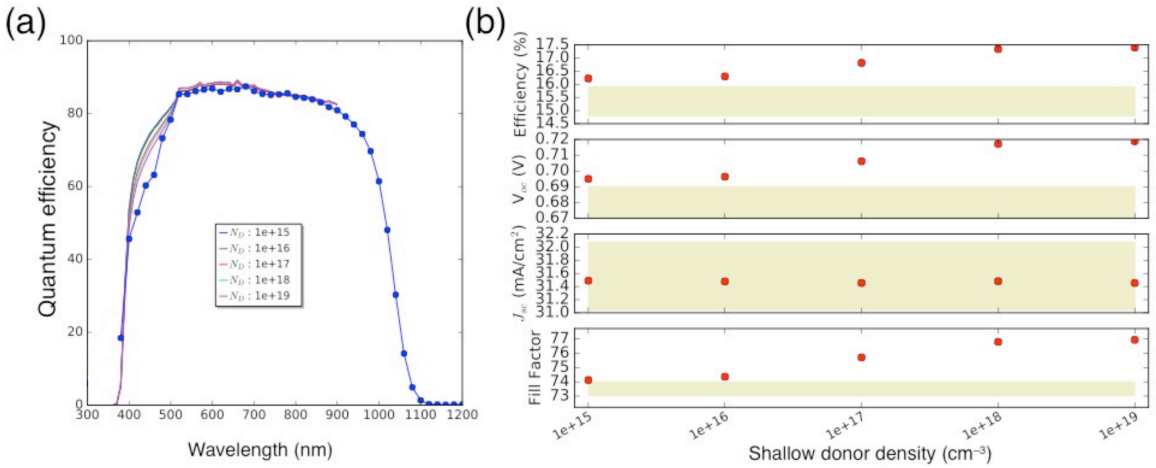

Figure 41. (a) Calculated quantum efficiency data for device model in SCAPS compared to the experimentally obtained data (blue points) for the standard process CIGS MiaSolé devices. The data is taken over a series of buffer shallow donor concentrations (1E15-1E19 cm^{-3}), which shows that degenerately doped buffers are one possible source for the observed shoulder in the experimental data. (b) A comparison of other important device performance metrics compared to the typical range of values obtained with manufactured devices (yellow band), which helps inform modifications to the underlying physics within the device model.

In Figure 42, we do a sensitivity analysis of the device performance to other buffer layer properties such as the band gap and the quality of the interface that are expected to be affected the different process conditions that yield different buffer alloy compositions. As expected, we find that increasing the buffer band gap can lead to a suppression of the observed shoulder and leads to only slightly higher device efficiencies overall. This reflects the initial motivation for identifying other buffer candidates that reduce unwanted absorption and yield improved collection of the photocurrent. In Figure 42(b) we find that increasing the trap density at the absorber-buffer interface and the associated interfacial hole recombination velocity (S_h), can also result in the observed shoulder in the QE and is correlated with a decrease in performance for interfacial trap densities exceeding 1E9 cm^{-2} assuming our other standard device parameters. Since our previous results on identify a large fraction of the CdZnOS alloy compositions which blue-shift the bandgap of CdS are expected to yield inferior interface qualities, we would generally expect this trend for the majority of CdZnOS and ZnOS alloys.

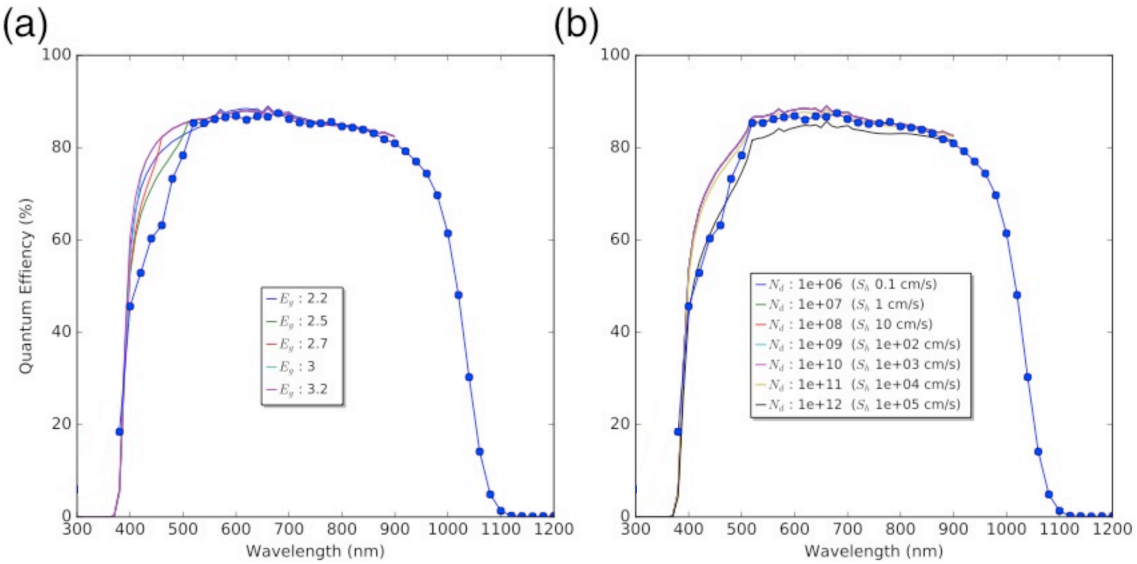

Figure 42. Calculated quantum efficiency data for device model in SCAPS compared to the experimentally obtained data (blue points) for the standard process CIGS MiaSolé devices for series over (a) a range of buffer band gaps and (b) a range of interfacial defect densities at the absorber-buffer interface. The results indicate two more possible origins for the features in the experimental QE data, in addition to the buffer doping concentration from Figure 41.

While these studies focus on modifying individual parameters like band gap and shallow donor concentration, we note that our calculations of the alloys indicate that many of the properties are strongly correlated and cannot be independently varied, at least within the CdZnOS system. For instance, the predicted increase in the interfacial recombination velocity could be offset by other advantages associated with a given alloy compositions, such as a more favorable conduction band offset or higher dopability as compared to CdS. This illustrates the complexity in device optimization and why these simulations are necessary to fully gauge how target alloy compositions may influence device efficiency. In Figure 43 we show the results for explicit models as parameterized from alloy compositions extracted from EDS measurements of the buffer. These measurements quantified the composition in certain regions and identified low Zn contents on the order of 5% and O contents ranging from ~10-20%, which we used to identify the relevant materials parameters for our buffer layer in the SCAPS simulation. Specifically, these compositions translate into a slight reduction in the conduction band offset and bandgap, a higher shallow donor concentration, and a drastically reduced interfacial recombination velocity as supported by the high crystalline quality observed in TEM measurements. In Figure 43(a) we see that the incorporation of O and Zn yields a better agreement in the qualitative features of the QE, while some of our device performance metrics like the V_{oc} in Figure 43(b) still appear slightly overestimated compared to the real device results. This discrepancy indicates that certain features are still missing from our model and motivates continued device level and experimental studies to improve the working model.

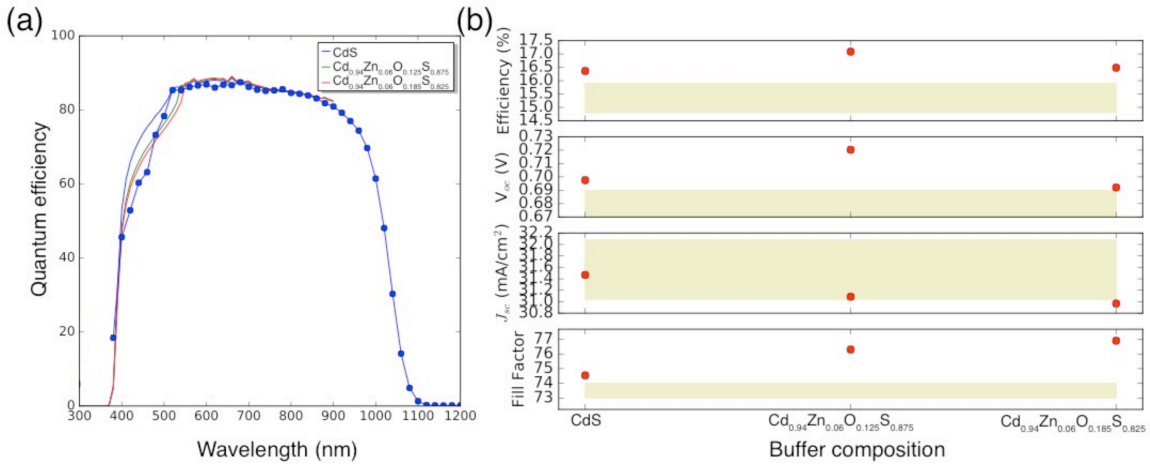

Figure 43. Calculated (a) quantum efficiency data and (b) performance parameters for different buffer compositions as implemented in our SCAPS device model and described in the text. The QE data in (a) is again compared to the experimental data (blue points) for the standard process CIGS MiaSolé devices. While features in the QE are better reproduced with CdZnOS alloys in (a), other device performance parameters are still overestimated with respect to experiment in (b) and indicate the need for additional modifications of the device model.

Conclusions

All project milestones and the go/no-go decision point were completed. In fact, we were able to go above and beyond the objectives for some tasks, as described above.

Among the most important electronic aspects of the absorber/buffer layer interface are the effective band lineup and the presence of point defects that influence charge transport, either as passive dopants or active recombination centers. The magnitude and sign of the band offsets affect carrier transport across the interface, while recombination centers may significantly deplete photocurrent. In addition, trapped charge at the interface can affect band bending, which is related to the band lineup. Typical devices nominally consist of a *p*-type CIGS absorber with a lightly *n*-type CdS buffer layer, however intermixing at the interface can be significant, which may affect both doping profile and distribution of impurities in both layers. Generally, a small positive conduction band offset from the *p*-type absorber to the *n*-type buffer is optimal.

Our theoretical work aimed to comprehensively address the properties of CdS to identify why it has been such a successful buffer layer, and to apply this knowledge to engineering improved buffer materials. Our initial work focused on establishing the flat-band offsets for ideal interfaces and and an understanding of the intrinsic tendency for certain electronic behavior in CdS and ZnS buffer materials based on the energetics of native defects and common impurities. The band offsets among $CuGaSe_2$, $CuInSe_2$, CdS, ZnS, and ZnO were computed at the screened hybrid functional level, giving very good agreement with experimental results where available, which provides confidence in the predictive ability of the theory. Defect states in the bulk of CdS (and ZnS) were compared to the computed band lineups to estimate the propensity for carrier trapping and/or recombination at the interface; intrinsic defects in both CdS and ZnS were found

to introduce potential recombination centers for photogenerated holes near the interface.

We also analyzed the effects of intermixing from the point of view of redistribution of elements as impurities in the buffer layer, particularly from CIGS or from the transparent conducting window layer like ZnO or SnO_2. For example, the electronic properties of relevant absorber-related impurities like Cu, Ga, In, Se, and common additives like Na and K were computed for CdS and ZnS to identify their effects at the heterojunction. These represent interdiffusion impurities from CIGS into CdS (with Na and K being intentionally diffused-in impurities) and are related to both short-term and long-term device performance and stability. The effects of these defects as recombination centers affecting charge transport were discussed, and their diffusivities were analyzed in relation to intermixing rates under various conditions. Experiments also demonstrated additional details of how growth conditions affect intermixing in both positive and negative ways, for example relating favorable Cd doping of the CIGS surface with oxygen in the sputter gas.

Lastly we spent considerable effort determining routes to engineering improved buffer layers through alloying. We mapped out the properties of CdZnOS quaternary solid solutions as a function of composition and identified alloys that may be favorable buffer layers in terms of the electronic and optical properties. We additionally considered their overall stability with respect to a number of competing phases that are known to form in real material depending on the process conditions.

Our results collectively have improved greatly our understanding of what makes a good buffer layer material stack and have provided valuable insight into developing more promising alternatives to pure CdS. We have identified several critical material parameters to maximize device efficiency. The specific details may depend on the precise absorber material, including any composition gradients, of a particular device technology, but the general paradigm to pushing a given technology to its efficiency maximum is the same. In summary, the knowledge gained toward a path to >21% efficient CIGS devices and recommendations on process options to advance the state of the art in that direction include:

- High crystallinity of the buffer material appears advantageous, by reducing interface defects and presumably reducing recombination losses in the bulk. A highly crystalline morphology may also promote the effective use of thinner buffer layers, which will reduce parasitic absorption.
- Cd doping of the CIGS surface layer seems beneficial, from comparison of devices showing different degrees of intermixing. Such doping can be most effective under conditions that promote Cu/Cd counter-doping across the CIGS/buffer interface. In cases where Cu diffusion leads to some CdS being replaced with a $Cu_{2-\delta}S$ compound, we observed little apparent degradation in performance related to that secondary phase in the buffer.
- Proper band alignment of the absorber and buffer is required for efficient carrier collection, as shown by our and previous device models. For *p*-type CIGS and a moderately *n*-type buffer, a small positive conduction band offset from the absorber to the buffer is generally optimal. Good composition control of the buffer

and the CIGS surface is required to achieve the desired band offset. However, we also find that real devices often incorporate complex composition gradients and phase segregated films, as opposed to discrete uniform layers assumed in typical device models. Further work on modeling realistic device stacks in 2D and 3D may be necessary to properly describe the effects of band offsets.

- Solar transparency of the buffer (a wide band gap with respect to the solar spectrum) is known to reduce parasitic losses, and accurate compositional control of the fabricated films is essential to reliably address this issue, as described above.

For the case of CdS-based buffers on CIGS absorbers, we find that a critical aspect is the incorporation of oxygen into the buffer material, which impacts several of the listed criteria. Control of O in the process is readily achieved with PVD, but is much more difficult with CBD. The amount of O incorporated controls crystallinity of the buffer, intermixing of Cd/Cu across the absorber/buffer interface, band gap, and band offset. Zinc incorporation can also fine-tune these effects, in particular the band gap and offset. Indeed, Zn incorporation is also partly controlled by O in the PVD process, as we observed a correlation between Zn incorporation from the ZnO window layer and O content in the process gas.

In general, we found that the final resulting materials can be different than the nominally deposited materials, due to complex elemental intermixing that can occur. Material characterization is required to uncover the specific resulting compositions, as we have done in this project. Careful process control is required to obtain the target composition profile. In the PVD process, oxygen again is one of the key process parameters. Doping of Cd into the CIGS surface layer is generally desirable, and the doping depth was found to be much greater using a PVD process than a CBD process, likely related to the higher temperatures used for PVD.

Regarding the MiaSolé device stacks studied in this project, we discovered that a near-optimal CdZnOS buffer alloy was stumbled upon through a long Edisonian processes, indeed with little chemical information available during the development. With the understanding now generated, an accelerated rational path forward is possible. Prior to this work, very little detailed chemical information was available to correlate with improved devices and little theoretical information was available to plan a rigorous path forward. In particular, previous models assumed discrete layers and ignored the significant intermixing and composition gradients now understood to exist. The path forward will aim for intentional control of these composition gradients, which must be included explicitly in device models.

Budget and Schedule

Total project budget was $945,000, including $900,000 federal share and $45,000 cost share (MiaSolé Hi-Tech). All funds were spent. The original schedule included two 18-month budget periods, beginning 1/1/2013 through 12/31/2015. Actual spending of the federal share against original plan is shown in Figure 44. Delayed spending at the beginning of the project was due to visa delays in hiring a microscopist postdoc. Reduced spending toward the end of 2015 and subsequent no-cost time extension

(NCTE) through 6/30/2016 allowed additional experimental cycles to take place at NCEM. An additional NCTE through 9/30/2016 allowed finalizing papers, this final report, and end-of-project conference travel to disseminate results. Project milestones were met on-time, despite schedule extensions, which enabled additional data to be gathered within the original budget constraints.

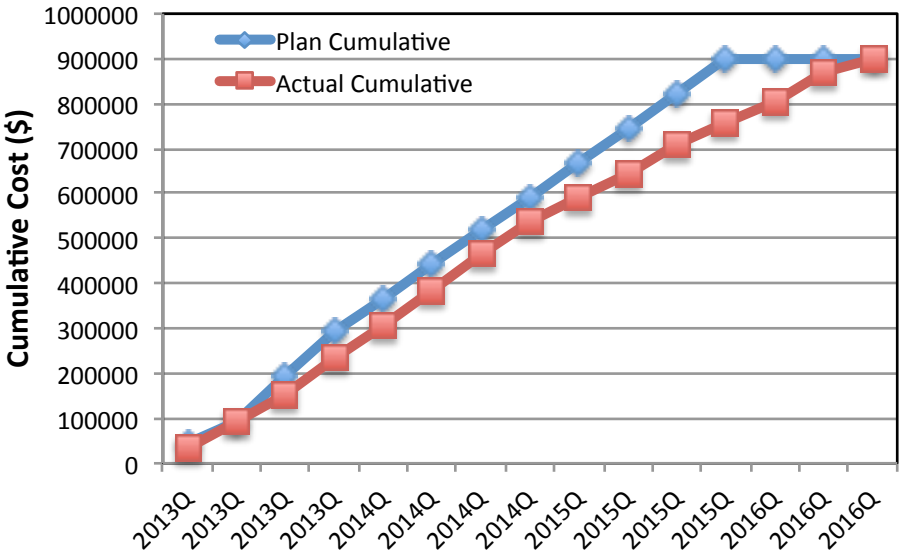

Figure 44. Spending rate of federal share against original budget plan.

Path Forward

Some of the team will continue related research as part of separately funded projects focusing on contact and absorber layers. Continued technology development based on this work will occur at MiaSolé Hi-Tech. Future funding opportunities to continue this direct line of research and development on the buffer and absorber/buffer interface would be welcome.

One joint patent application has been filed, both in the U.S. and China, regarding process control during sputter deposition of alloyed buffers; see listing in **Publications Resulting from Project** section.

References

1 X. Wu, *et al.*, “16.5%-Efficient CdS/CdTe Polycrystalline Thin-film Solar Cell,” *Proceedings, 17th European Photovoltaic Solar Energy Conference,* Munich, 995-1000 (2011).

2 P. Jackson, *et al.*, “New World Record Efficiency for Cu(In,Ga)Se_2 Thin-film Solar Cells,” *Prog. Photovolt*. (2011).

3 T. Todorov, K. Reuter and D. Mitzi, “High-Efficiency Solar Cell with Earth-Abundant Liquid-Processed Absorber," *Adv. Materials* **22**, E156-E159 (2012).

[4] S. Siebentritt, "What Limits the Efficiency of Chalcopyrite Solar Cells?" *Sol. Energy. Mat. Sol. Cells* **95**, 1471-1476 (2011).

[5] B. McCandless and J. Sites, "Cadmium Telluride Solar Cells," in *Handbook of Photovoltaic Science and Engineering* (Wiley, 2003), p. 653.

[6] N. Naghavi, *et al.*, "Buffer Layers and Transparent Conducting Oxides for Chalcopyrite Cu(In,Ga)(S,Se)$_2$ Based Thin-film Photovoltaics: Present Status and Current Developments," *Prog. Photovolt*. **18**, 411-433 (2010); and references therein.

[7] R.N. Battacharya, *et al*., "High efficiency thin-film $CuIn_{1-x}Ga_xSe_2$ photovoltaic cells using a $Cd_{1-x}Zn_xS$ buffer layer," *Applied Physics Letters* **89**, 253503 (2006).

[8] T. Nakada, M. Mizutani, Y. Hagiwara and A. Kunioka, "High-efficiency Cu(In,Ga)Se$_2$ Thin-film Solar Cells with a CBD-ZnS Buffer Layer," *Sol. Energy. Mat. Sol. Cells* **67**, 255-260 (2001).

[9] C. Platzer-Bjorkman, T. Torndahl, A. Hultqvist, J. Kessler and M. Edoff, "Optimization of ALD-(Zn,Mg)O Buffer Layers and (Zn,Mg)O/Cu(In,Ga)Se$_2$ Interfaces for Thin-film Solar Cells," *Thin Solid Films* **515**, 6024-6027 (2007).

[10] R. Scheer, "Activation Energy of Heterojunction Diode Currents in the Limit of Interface Recombination," *J. Appl. Phys.* **105**, 104505 (2009).

[11] C. Platzer-Bjorkman, et al., "Zn(O,S) buffer layers by atomic layer deposition in Cu(In,Ga)Se$_2$ Based Thin-film Solar Cells: Band Alignment and Sulfur Gradient." *J. Appl. Phys*. **100**, 044506 (2006).

[12] A. Niemegeers, M. Burgelman and A. De Vos, "On the CdS/CuInSe2 Conduction Band Discontinuity,"*Appl. Phys. Lett*. **67**, 843 (1995).

[13] Q. Nguyen, *et al.*, "Influence of Heterointerfaces on the Performance of Cu(In,Ga)Se$_2$ Solar Cells with CdS and In(OH,S) Buffer Layers," *Thin Solid Films* **431-432**, 330-334 (2003).

[14] T. Nakada and A. Kunioka, "Direct evidence of Cd diffusion into Cu(In,Ga)Se$_2$ thin films during chemical-bath deposition process of CdS films," *Applied Physics Letters,* vol. 74, pp. 2444-2446 (1999).

[15] K. Kushiya, *et al.*, "Improved FF of CIGS Thin-film Mini-modules with Zn(O,S,OH)$_x$ Buffer by Post-deposition Light Soaking," *Proceedings, 26th IEEE Photovoltaics Specialist Conf.,* Anaheim, (1997).

[16] A. Pudov, J. Sites, M. Contreras, T. Nakada and H. Schock, "CIGS J-V Distortion in the Absence of Blue Photons," *Thin Solid Films* **480-481**, 273-278 (2005).

[17] A. Pudov, A. Kanevce, H. Al-Thani, J. Sites and F. Hasoon, "Secondary Barriers in CdS - CuInGaSe Solar Cells," *J. Appl. Phys*. **97**, 064901 (2005).

[18] S. Lany and A. Zunger, "Light- and Bias-induced Metastabilities in Cu(In,Ga)Se$_2$ Based Solar Cells Caused by the (V_{Se}-V_{Cu}) Vacancy Complex." *J. Appl. Phys.* **100**, 113725 (2006).

[19] G. Brown, V. Faifer, A. Pudov, B. Cardozo and D. Jackrel, "Quantitative Measurements of Electronic Nonuniformities in Thin-film Photovoltaics and their Impact on Device Performance," *Proceedings, 37th IEEE Photovoltaics Specialist Conference,* Seattle, (2011).

[20] J. Heyd, G. E. Scuseria, and M. Ernzerhof, J. Chem. Phys. 118, 8207 (2003); 124, 219906 (2006).

[21] G. Kresse and J. Furthmüller, Phys. Rev. B 54, 11169 (1996); Comput. Mater. Sci. 6, 15 (1996).

[22] J.P. Perdew, K. Burke, K., and M. Ernzerhof, Phys. Rev. Lett. 77, 3865 (1996).

[23] C. Freysoldt, J. Neugebauer, and C. G. Van de Walle, Phys. Rev. Lett. 102, 016402 (2009); phys. stat. sol. (b) 248, 1067 (2010).

[24] O. Madelung, *Semiconductors: Data Handbook*, 3rd ed. (Springer-Verlag, New York, NY, 2004).

[25] C.G. Van de Walle and J. Neugebauer, J. Appl. Phys. 95, 3851 (2004).

[26] G. Henkelman, B.P. Uberuaga, and H.Jonsson, J. Chem. Phys. 113, 9901 (2000).

[27] J. von Pezold, A. Dick, M. Friák, and J. Neugebauer, "Generation and performance of special quasirandom structures for studying the elastic properties of random alloys: Application to Al-Ti," *Phys. Rev. B*, vol. 81, no. 9, p. 094203 (2010).

[28] J.-C. Wu, J. Zheng, C. L. Zacherl, P. Wu, Z.-K. Liu, and R. Xu, "Hybrid Functionals Study of Band Bowing, Band Edges and Electronic Structures of $Cd_{1-x}Zn_xS$ Solid Solution," *J. Phys. Chem. C*, vol. 115, no. 40, pp. 19741–19748, (2011).

[29] P.D.C. King and T.D. Veal, J. Phys.: Condens. Matter 23, 334214 (2011).

[30] A. Schleife, F. Fuchs, C. Rödl, J. Furthmüller, and F. Bechstedt, Appl. Phys. Lett. 94, 012104 (2009).

[31] J.B. Varley and V. Lordi, "Electrical properties of point defects in CdS and ZnS," *Appl. Phys. Lett.* 103, 102103 (2013).

[32] J.B. Varley, V. Lordi, X. He, and A. Rockett, "First principles calculations of point defect diffusion in CdS buffer layers: Implications for $Cu(In,Ga)(Se,S)_2$ and $Cu_2ZnSn(Se,S)_4$-based thin-film photovoltaics," Journal of Applied Physics, 119, 25703 (2016).

[33] J.B. Varley and V. Lordi, "Intermixing at the absorber-buffer layer interface in thin-film solar cells: The electronic effects of point defects in Cu(In,Ga)(Se,S)2 and Cu2ZnSn(Se,S)4 devices," Journal of Applied Physics, 116, 063505 (2014).

[34] B.K. Meyer and W. Stadler, "Native defect identification in II–VI materials," *J. Cryst. Growth*, vol. 161, no. 1, pp. 119–127, 1996.

[35] U.V. Desnica, Prog. Cryst. Growth Charact. Mater. 36, 291 (1998).

[36] L. Weinhardt, M. Bär, S. Pookpanratana, M. Morkel, T. P. Niesen, F. Karg, K. Ramanathan, M. A. Contreras, R. Noufi, E. Umbach, and C. Heske, "Sulfur gradient-

driven Se diffusion at the CdS/CuIn(S,Se)[sub 2] solar cell interface," Appl. Phys. Lett., 96, 182102 (2010).

[37] A. Janotti and C.G. Van de Walle, Nature Materials 6, 44 (2006).

[38] S. Lany and A. Zunger, "Anion vacancies as a source of persistent photoconductivity in II-VI and chalcopyrite semiconductors," Phys. Rev. B, 72, 035215 (2005).

[39] C. Heske, D. Eich, R. Fink, E. Umbach, T. van Buuren, C. Bostedt, L. J. Terminello, S. Kakar, M. M. Grush, T. A. Callcott, F. J. Himpsel, D. L. Ederer, R. C. C. Perera, W. Riedl, and F. Karg, "Observation of intermixing at the buried CdS/Cu(In,Ga)Se_2 thin film solar cell heterojunction," Appl. Phys. Lett., 74, 1451 (1999).

[40] M. Bär, S. Nishiwaki, L. Weinhardt, S. Pookpanratana, O. Fuchs, M. Blum, W. Yang, J. D. Denlinger, W. N. Shafarman, and C. Heske, "Depth-resolved band gap in Cu(In,Ga)(S,$Se)_2$ thin films," Appl. Phys. Lett., 93, 244103 (2008).

[41] A. Chirilă, P. Reinhard, F. Pianezzi, P. Bloesch, A. R. Uhl, C. Fella, L. Kranz, D. Keller, C. Gretener, H. Hagendorfer, D. Jaeger, R. Erni, S. Nishiwaki, S. Buecheler, and A. N. Tiwari, "Potassium-induced surface modification of Cu(In,Ga)Se_2 thin films for high-efficiency solar cells," Nature Materials, 12, 1107 (2013).

[42] J. Hedström, H. Ohlsen, M. Bodegård, A. Kylner, L. Stolt, D. Hariskos, R. M, and H.-W. Schock, "ZnO/CdS/Cu(In,Ga)Se_2 thin film solar cells with improved performance," presented at the 23rd IEEE Photovoltaic Specialists Conference, pp. 364–371 (1997).

[43] L. E. Oikkonen, M. G. Ganchenkova, A. P. Seitsonen, and R. M. Nieminen, "Effect of sodium incorporation into CuInSe2 from first principles," J. Appl. Phys.,114, 083503 (2013).

[44] W. Liu, J.-J. He, Z.-G. Li, W.-L. Jiang, J.-B. Pang, Y. Zhang, and Y. Sun, "Effect of Na on lower open circuit voltage of flexible CIGS thin-film solar cells prepared by the low-temperature process," Phys. Scr., 85, 055806 (2012).

[45] W.D. Gill and R.H. Bube, "Photovaltaic properties of CdS/Cu_2S heterojunctions," *Journal of Applied Physics,* vol. 41, pp. 3731-3738 (1970).

[46] C. Rincon, R. Marquez, "Defect physics of the CuInSe2 chalcopyrite semiconductor," *J. Phys. Chem. Solids,* vol. 60, pp. 1865–1873 (1999).

[47] P. Lukashev, W. Lambrecht, T. Kotani, and M. V. Schilfgaarde, "Electronic and crystal structure of Cu2-xS: Full-potential electronic structure calculations," *Phys. Rev. B*, vol 76. p. 195202 (2007).

[48] T. Nakada, "Nano-structural investigations on Cd-doping into Cu(In,Ga)Se_2 thin films by chemical bath deposition process," *Thin Solid Films,* vol. 361, pp. 346-352 (2000).

[49] D. Abou-Ras, G. Kostorz, A. Romeo, D. Rudmann, and A. Tiwari, "Structural and chemical investigations of CBD- and PVD-CdS buffer layers and interfaces in Cu(In,Ga)Se_2-based thin film solar cells," *Thin Solid Films,* vol. 480, pp. 118-123 (2005).

[50] M.G. Hall, H.I. Aaronson, and K.R. Kinsma, "The structure of nearly coherent fcc: bcc boundaries in a Cu-Cr alloy," *Surface Science,* vol. 31, pp. 257-274 (1972).

[51] C. Persson and A. Zunger, "Anomalous Grain Boundary Physics in Polycrystalline $CuInSe_2$: The Existence of a Hole Barrier," *Physical Review Letters,* vol. 91, p. 266401 (2003).

[52] S. Siebentritt, S. Sadewasser, M. Wimmer, C. Leendertz, T. Eisenbarth, and M. C. Lux-Steiner, "Evidence for a Neutral Grain-Boundary Barrier in Chalcopyrites," *Physical Review Letters,* vol. 97, p. 146601 (2006).

[53] Y. Yan, R. Noufi, and M. M. Al-Jassim, "Grain-Boundary Physics in Polycrystalline $CuInSe_2$ Revisited: Experiment and Theory," *Physical Review Letters,* vol. 96, p. 205501 (2006).

[54] Y. Yan, C. S. Jiang, R. Noufi, S.-H. Wei, H. R. Moutinho, and M. M. Al-Jassim, "Electrically Benign Behavior of Grain Boundaries in Polycrystalline $CuInSe_2$ Films," *Physical Review Letters,* vol. 99, p. 235504 (2007).

[55] D. Abou-Ras, B. Schaffer, M. Schaffer, S. S. Schmidt, R. Caballero, and T. Unold, "Direct Insight into Grain Boundary Reconstruction in Polycrystalline $Cu(In,Ga)Se_2$ with Atomic Resolution," *Physical Review Letters*, 108(7), 075502 (2012).

[56] D. X. Liao and A. Rockett, "Cd doping at the CuInSe2/CdS heterojunction," *Journal of Applied Physics,* vol. 93, pp. 9380-9382 (2003).

[57] K. Ramanathan, R. Noufi, J. Granata, J. Webb, and J. Keane, "Prospects for in situ junction formation in CuInSe2 based solar cells," *Solar Energy Materials and Solar Cells,* vol. 55, pp. 15-22 (1998).

[58] K.W. Boer, "The CdS/Cu_2S solar-cell," *Journal of Crystal Growth,* vol. 59, pp. 111-120 (1982).

[59] J. Park, S. Heo, J.-G. Chung, H. Kim, H. Lee, K. Kim, and G.-S. Park, Ultramicroscopy **109** (9), 1183 (2009).

[60] V. Nadenau, D. Hariskos, H. W. Schock, M. Krejci, F. J. Haug, A. N. Tiwari, H. Zogg, and G. Kostorz, "Microstructural study of the CdS/CuGaSe2 interfacial region in CuGaSe2 thin film solar cells," *Journal of Applied Physics,* vol. 85, pp. 534-542, (1999).

[61] O. Cojocaru-Miredin, P. Choi, R. Wuerz, and D. Raabe, "Exploring the p-n junction region in Cu(In,Ga)Se-2 thin-film solar cells at the nanometer-scale," *Applied Physics Letters,* vol. 101, 181603 (2012).

[62] S. J. Pennycook, "Z-contrast STEM for materials science," *Ultramicroscopy,* vol. 30, pp. 58-69 (1989).

[63] S.B. Zhang and S.H. Wei, "Reconstruction and energetics of the polar (112) and (-1-1-2) versus the nonpolar (220) surfaces of $CuInSe_2$," *Physical Review B,* vol. 65, 081402(R) (2002).

[64] S.D. Findlay, T. Saito, N. Shibata, Y. Sato, J. Matsuda, K. Asano, E. Akiba, T. Hirayama, and Y. Ikuhara, "Direct Imaging of Hydrogen within a Crystalline Environment," *Applied Physics Express,* 3, 116603 (2010).

[65] X. He, L. Gu, C. Zhu, Y. Yu, C. Li, Y.-S. Hu, H. Li, S. Tsukimoto, J. Maier, Y. Ikuhara, and X. Duan, "Direct Imaging of Lithium Ions Using Aberration-Corrected Annular-Bright-Field Scanning Transmission Electron Microscopy and Associated Contrast Mechanisms," *Materials Express,* vol. 1, pp. 43-50 (2011).

[66] A. Chirila, P. Reinhard, F. Pianezzi, P. Bloesch, A. R. Uhl, C. Fella, L. Kranz, D. Keller, C. Gretener, H. Hagendorfer, D. Jaeger, R. Erni, S. Nishiwaki, S. Buecheler, and A. N. Tiwari, "Potassium-induced surface modification of Cu(In,Ga)Se-2 thin films for high-efficiency solar cells," *Nature Materials,* vol. 12, pp. 1107-1111 (2013).

[67] N.M. Mangan, R.E. Brandt, V. Steinmann, R. Jaramillo, C. Yang, J.R. Poindexter, R. Chakraborty, H.H. Park, X. Zhao, R.G. Gordon and T. Buonassisi, "Framework to predict optimal buffer layer pairing for thin film solar cell absorbers: A case study for tin sulfide/zinc oxysulfide," *J. Appl. Phys*. 118, 115102 (2015).

[68] S.B. Zhang, S. Wei, and A. Zunger, "A phenomenological model for systematization and prediction of doping limits in II-VI and I-III-VI_2 compounds," *J. Appl. Phys.* 83, 6 (1998).

[69] R.E. Brandt, M. Young, H.H. Park, A. Dameron, D. Chua, Y.S. Lee, G. Teeter, R.G. Gordon, and T. Buonassisi, "Band offsets of n-type electron-selective contacts on cuprous oxide (Cu2O) for photovoltaics," *Appl. Phys. Lett.*, 105, 263901, (2014).

[70] X. Wu, R.G. Dhere, Y. Yan, M.J. Romero, Y. Zhang, J. Zhou, C. DeHart, A. Duda, C. Perkins, and B. To, "High-efficiency polycrystalline CdTe thin-film solar cells with an oxygenated amorphous CdS (a-CdS: O) window layer," pp. 531–534 (2002).

[71] A. Klein, "Energy band alignment in chalcogenide thin film solar cells from photoelectron spectroscopy," *J. Phys.: Condens. Matter*, vol. 27, no. 13, p. 134201 (2015).

[72] D. A. Duncan, J.M. Kephart, K. Horsley, M. Blum, M. Mezher, L. Weinhardt, M. Häming, R. G. Wilks, T. Hofmann, W. Yang, M. Bär, W. S. Sampath, and C. Heske, "Characterization of Sulfur Bonding in CdS:O Buffer Layers for CdTe-based Thin-Film Solar Cells," *ACS Appl. Mater. Interfaces*, 7, 16382 (2015).

[73] Q. Xu, B. Huang, Y. Zhao, Y. Yan, R. N. Noufi, and S.-H. Wei, "Crystal and electronic structures of Cu_xS solar cell absorbers," *Appl. Phys. Lett.*, 100, 061906 (2012).

Publications Resulting from Project

Published Journal Articles

1. J.B. Varley and **V. Lordi**, "Electrical properties of point defects in CdS and ZnS," *Applied Physics Letters* 103, 102103 (2013).

2. J.B. Varley and **V. Lordi**, "Intermixing at the absorber-buffer layer interface in thin-film solar cells: The electronic effects of point defects in $Cu(In,Ga)(Se,S)_2$ and $Cu_2ZnSn(Se,S)_4$ devices," *Journal of Applied Physics,* 116, 063505 (2014).
3. X.Q. He, G. Brown, K. Demirkan, N. Mackie, V. Lordi, and A. Rockett, "Microstructural and chemical investigation of PVD-CdS/PVD-$CuIn_{1-x}Ga_xSe_2$ heterojunctions: a transmission electron microscopy study," IEEE Journal of Photovoltaics, 4, 1625 (2014).
4. J.B. Varley, V. Lordi, X. He, and A. Rockett, "First principles calculations of point defect diffusion in CdS buffer layers: Implications for $Cu(In,Ga)(Se,S)_2$ and $Cu_2ZnSn(Se,S)_4$-based thin-film photovoltaics," Journal of Applied Physics, 119, 25703 (2016).
5. X. He, J. Varley, P. Ercius, T. Erikson, J. Bailey, G. Zapalac, D. Poplavskyy, N. Mackie, A. Bayman, V. Lordi and A. Rockett, "Cu rich domains and secondary phases in PVD-CdS/PVD-$CuInGaSe_2$ heterojunctions," IEEE J. of Photovoltaics, JPV-2016-04-0141-R (2016).
6. X. He, J. Varley, P. Ercius, T. Erikson, J. Bailey, G. Zapalac, D. Poplavskyy, N. Mackie, A. Bayman, V. Lordi and A. Rockett, "Intermixing and formation of Cu-rich secondary phases at sputtered CdS/$CuInGaSe_2$ heterojunctions," IEEE J. of Photovoltaics, *in press* (2016). DOI: 10.1109/JPHOTOV.2016.2589362

In-Preparation Journal Articles

1. X.Q. He, T. Paulauskas, P. Ercius, J. Varley, J. Bailey, G. Zapalac, T. Nagle, D. Poplavskyy, N. Mackie, A. Bayman, R. Klie, V. Lordi, and A. Rockett, "Cd doping at PVD-CdS/$CuInGaSe_2$ heterojunctions," *in preparation* (2016).
2. X.Q. He, P. Ercius, J.B. Varley, J. Bailey, G. Zapalac, T. Nagle, D. Poplavskyy, N. Mackie, A. Bayman, V. Lordi, and A. Rockett, "The role of oxygen doping on elemental intermixing at the PVD-CdS/$CuIn_{1-x}GaxSe_2$ heterojunction," *in preparation* (2016).
3. J.B. Varley, X.Q. He, A. Rockett, and V. Lordi, "The stability of $Cd_{1-x}Zn_xO_yS_{1-y}$ quaternary alloys assessed with first principles calculations," *in preparation* (2016).
4. J.B. Varley, X.Q. He, A. Rockett, and V. Lordi, "Exploring Cd-Zn-O-S alloys as optimal buffer layers for thin-film photovoltaics," *in preparation* (2016).
5. J.B. Varley and V. Lordi, "Extrinsic defects in CdS and ZnS buffers grown by chemical bath deposition," *in preparation* (2016).

Conference Presentations (5 invited)

1. J.B. Varley and V. Lordi; "Electrical Properties of Point Defects in CdS from First Principles;" OP203; SPIE Optics+Photonics; San Diego, CA; August 27-29, 2013.
2. J.B. Varley and V. Lordi; "Electrical Properties of Point Defects in CdS and ZnS from First Principles;" A5.09; Photovoltaic Materials and Manufacturing III: Materials Research Society Technology Development Workshop; Golden, CO; Sept 10-13, 2013.

3. J.B. Varley and V. Lordi; “Electrical Properties of Point Defects in CdS from First Principles;” WW8.04; MRS Fall Meeting; Boston, MA; Dec 1-6, 2013.
4. J.B. Varley and V. Lordi; “Electrical Properties of Point defects in CdS and ZnS Thin-Film PV Buffer Layers;” TMS Annual Meeting; San Diego, CA; Feb 16-20, 2014.
5. J.B. Varley and V. Lordi; “Defects in Buffer Layers: Electrical and Optical Properties of Point Defects in CdS and ZnS;” F24.10; American Physical Society March Meeting; Denver, CO; March 3-7, 2014.
6. J.B. Varley and V. Lordi; “Intermixing at the Absorber-Buffer Interface in Thin-Film Photovoltaics;” H5.03; MRS Spring Meeting; San Francisco, CA; April 21-25, 2014.
7. X.Q. He, G. Brown, K. Demirkan, N. Mackie, V. Lordi, and A. Rockett; “Microstructural and chemical investigation of PVD-CdS/PVD-$CuIn_{1-x}Ga_xSe_2$ (CIGS)heterojunctions: a transmission electron microscopy study;” 40th IEEE Photovoltaic Specialists Conference; Denver, CO; June 8-13, 2014.
8. J.B. Varley, X.Q. He, N. Mackie, A. Rockett, and V. Lordi; “Intermixing at the absorber-buffer interface in thin-film photovoltaics;” H6; 56th Electronic Materials Conference; Santa Barbara, CA; June 25-27, 2014.
9. **(invited)** V. Lordi; “(Cd,Zn)(O,S) Buffer Materials for CIGS Solar Cell;” SunShot 3rd Thin-Film PV Workshop; Newark, DE; October 20-21, 2014.
10. J.B. Varley, X.Q. He, N. Mackie, A. Rockett, and V. Lordi; “Kinetic aspects of intermixing at the absorber-buffer interface in $Cu(In,Ga)Se_2$ thin-film photovoltaics;” V6.04; MRS Fall Meeting; Boston, MA; November 30-December 5, 2014.
11. **(invited)** J.B. Varley; “Optimizing buffer layers for high-efficiency thin-film photovoltaics;” UC-Santa Barbara Materials Department Seminar; Santa Barbara, CA; November 20, 2014.
12. J. Varley, X. He, N. Mackie, A. Rockett, V. Lordi; “Exploring Cd-Zn-O-S alloys for optimal buffer layers in thin-film photovoltaics;” J14.7; APS March Meeting; San Antonio, TX; March 2-5, 2015.
13. J.B. Varley, X. He, N. Mackie, A. Rockett, and V. Lordi; “Exploring CdZnOS alloys for optimal buffer layers in thin-film photovoltaics;” B9.07 (poster); Materials Research Society Spring Meeting; San Francisco, CA; April 6-10, 2015.
14. X.Q. He, P. Ercius, J. Bailey, G. Zapalac, N. Mackie, A. Bayman, J.B. Varley, V. Lordi, and A. Rockett; “Cu rich domains and secondary phases in PVD-CdS/ PVD-$CuIn_{1-x}Ga_xSe_2$ heterojunctions;” paper 47; 42nd IEEE Photovoltaic Specialist Conference; New Orleans, LA; June 14-19, 2015.
15. J.B. Varley, X. He, N. Mackie, A. Rockett, and V. Lordi; “Cd-Zn-O-S alloys for optimal buffer layers in thin-film photovoltaics;” 9561-10; SPIE Optics+Photonics; San Diego, CA; Aug 9-13, 2015.
16. J.B. Varley, X. He, N. Mackie, A. Rockett, and V. Lordi; “CdZnOS alloys for optimal buffer layers in thin-film photovoltaics;” 4th DOE SunShot Thin-Film Photovoltaic Workshop; Golden, CO; Aug 19-20, 2015.

17. J.B Varley, V. Lordi, X. He, A. Rockett, J. Bailey, G. Zapalac, N. Mackie, D. Poplavskyy; “Consequences of Impurity Incorporation in Chemical Bath Deposited CdS and ZnS Buffer Layers for Thin-Film Photovoltaics;” NN6.04; MRS Fall Meeting; Boston, MA; Nov 29-Dec 4, 2015.
18. **(invited)** V. Lordi; “Computational Studies of Materials Interfaces for Optimization of Energy Storage and Conversion Devices;” ENRG 584; PacifiChem 2015; Honolulu, HI, Dec 15-20, 2015.
19. **(invited)** V. Lordi; “Computational Studies of Materials Interfaces for Optimization of Energy Storage and Conversion Devices;” UC Davis Condensed Matter Physics Seminar; Davis, CA; April 28, 2016.
20. V. Lordi; “Design of Optimal Buffer Layers for CIGS Thin-Film Solar Cells;” HH2; Electronic Materials Conference; Newark, DE; June 22-24, 2016.
21. V. Lordi, J. Varley, X.Q. He, A. Rockett, J. Bailey, G. Zapalac, N. Mackie, D. Poplavskyy, A. Bayman; “Design of Optimal Buffer Layers for CIGS Thin-Film Solar Cells;” 9936-12; SPIE Optics+Photonics; San Diego, CA; Aug 28-Sept 1, 2016.
22. V. Lordi, J. Varley, X.Q. He, A. Rockett, J. Bailey, G. Zapalac, N. Mackie, D. Poplavskyy, A. Bayman; “Optimization of Buffer Layer Alloy Materials for CIGS Thin-Film Solar Cells;” TMS Annual Meeting; San Diego, CA; Feb 6-Mar 2, 2017.
23. **(invited)** V. Lordi; “Design of Optimal Buffer Layers for CIGS Thin-Film Solar Cells;” MRS Spring Meeting; Phoenix, AZ; Apr 17-21, 2017.

Patents Filed

1. N. Mackie, G. Zapalac, W. Zhang, J. Corson, X. He, A. Rockett, J. Varley, and V. Lordi, “Hexagonal Phase Epitaxial Cadmium Sulfide on Copper Indium Gallium Selenide for a Photovoltaic Junction,” provisional filed 5/15/2015, US application #62162371; PRC (China) application # 201610319278.4.